

F2former: When Fractional Fourier Meets Deep Wiener Deconvolution and Selective Frequency Transformer for Image Deblurring

Subhajit Paul¹, Sahil Kumawat², Ashutosh Gupta¹, Deepak Mishra²

¹Space Applications Centre (SAC), Ahmedabad

²Indian Institute of Space Science and Technology (IIST), Trivandrum

{subhajitpaul, ashutoshg}@sac.isro.gov.in, {sahil.sc21b114, deepak.mishra}@iist.ac.in

Abstract

Recent progress in image deblurring techniques focuses mainly on operating in both frequency and spatial domains using the Fourier transform (FT) properties. However, their performance is limited due to the dependency of FT on stationary signals and its lack of capability to extract spatial-frequency properties. In this paper, we propose a novel approach based on the Fractional Fourier Transform (FRFT), a unified spatial-frequency representation leveraging both spatial and frequency components simultaneously, making it ideal for processing non-stationary signals like images. Specifically, we introduce a Fractional Fourier Transformer (F2former), where we combine the classical fractional Fourier based Wiener deconvolution (F2WD) as well as a multi-branch encoder-decoder transformer based on a new fractional frequency aware transformer block (F2TB). We design F2TB consisting of a fractional frequency aware self-attention (F2SA) to estimate element-wise product attention based on important frequency components and a novel feed-forward network based on frequency division multiplexing (FM-FFN) to refine high and low frequency features separately for efficient latent clear image restoration. Experimental results for the cases of both motion deblurring as well as defocus deblurring show that the performance of our proposed method is superior to other state-of-the-art (SOTA) approaches.

1. Introduction

Image deblurring is an active research field in computer vision where it aims to restore high-quality clean data from real-world blurry observed data. It can be formulated as,

$$y = k * x + n, \quad (1)$$

where, y is the observed blurry input image, x is the clean image, k refers to the blur kernel, n is associated noise, and $*$ is the convolution operator. Traditional methods

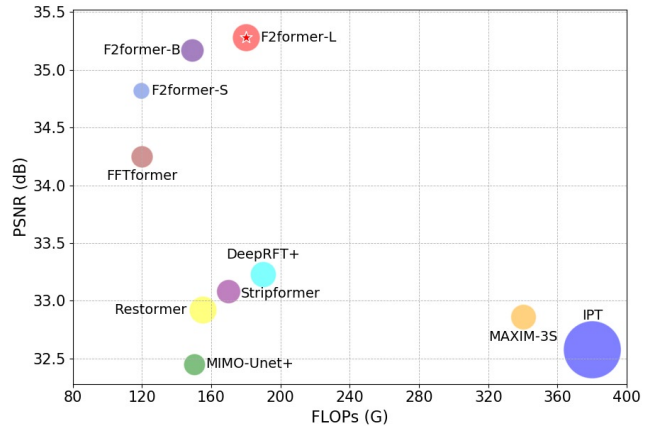


Figure 1. Comparison of the proposed model with other SOTA methods on the GoPro test dataset in terms of PSNR, floating point operations (FLOPs), and number of network parameters which are corresponded by the area of the circle.

tackled the problem of image blur through an estimation of k . Among them, early blind kernel estimation methods [20] mainly revolve around the concept of Wiener filter [45]. Later works focused on developing probabilistic approaches to formulate image priors [19, 47], and optimization-oriented nonblind kernel estimation methods [34, 35]. Although such methods are theoretically feasible, their practical appeal is limited for real world images with large variations in blur and noise statistics.

Recent deblurring methods typically employ deep learning (DL) models that operate in both frequency and spatial domains. These methods are usually restrained from using the information of blur pattern, resulting in limited performance. Some methods [14, 37] utilize this information in their DL models, achieving efficient performance. However, they are mostly effective under the uniform blur conditions. In real-world scenarios, such methods heavily fail due to the inability of the Fourier Transform (FT) to handle spatially varying non-uniform blur, as such cases require anal-

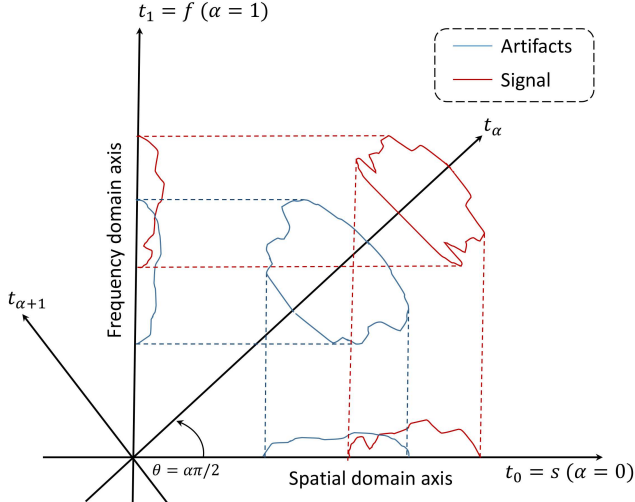


Figure 2. For optimal choice of α , FRFT inherently separates spatially varying artefacts from non-stationary signals along the fractional order axis t_α .

ysis of joint distribution between spatial and frequency domain information. Although short-time Fourier transform (STFT) [13] and wavelet transform (WT) [15] serve this purpose, STFT has issues related to properly balance spatial and frequency resolution and WT suffers from optimal choice of wavelet function and higher computational complexity.

To address this, we explore Fractional Fourier Transform (FRFT), a generalized version of FT and a unified spatial-frequency analysis tool. This can be visualized by applying a fractional exponent α to the basis of regular FT providing a linear transformation with angle $\theta = \frac{\alpha\pi}{2}$ with respect to the time axis in the time-frequency domain as shown in Figure 2. Hence, FRFT with a fractional order α offers an intermediate representation between spatial and frequency domains, effectively extracting spatially varying artefacts from non-stationary signals like images as shown in Figure 2.

In this paper, we propose Fractional Fourier based transformer (F2former) for effective image deblurring using FRFT. We design an FRFT based Wiener filter to perform deconvolution at the feature level to obtain sharp representations. To effectively reconstruct the deblurred image from these sharp features, we further employ FRFT based feature extractor and transformer blocks in a U-Net like encoder-decoder model. We develop these transformer blocks by computing frequency aware element-wise product attention at FRFT domain and extracting high and low frequency elements to selectively restore significant components in Fourier domain. Our model yields favorable results in both PSNR as well as efficiency on the benchmark dataset, GoPro as shown in Figure 1. Our main contribu-

tions are as follows,

- A *Fractional Feature-based Wiener Deconvolution* (F2WD) layer to enhance the shallow-level features given a blurry input. As FRFT is capable of capturing spatially varying artefacts, F2WD efficiently performs deblurring in feature space.
- We develop a novel building block, *Fractional Hybrid Transformer Block* (FHTB) to efficiently reconstruct the deblurred image. FHTB is composed of **F**ractional **F**ourier based **F**eature **R**efinement module (F3RB) and also a **T**ransformer **B**lock (F2TB) to extract local and global context features, respectively.
- We design F2TB with *Fractional Frequency aware Self-Attention* (F2SA) for efficient computation and selective emphasis on key frequency components, and *Frequency Division Multiplexing-based FFN* (FM-FFN) to dynamically extract high and low frequency features using a cosine bell function for optimal frequency recovery.
- We conduct experiments to demonstrate the effectiveness of the proposed F2former for motion and defocus blurring, showing significant performance improvements over other SOTA models. We also provide a detailed ablation study to validate the contribution of each module.

2. Related Work

2.1. Deep learning based deblurring methods

Recently, many DL based effective image deblurring methods have emerged. This include both CNN based [5, 9, 54], and transformer based approaches [6, 17, 43, 44, 53]. However, as convolution operation in CNN is spatially invariant, it does not capture global context for image restoration tasks resulting in limited performance. In this regard, transformer based models make substantial progress in numerous high-level vision tasks [3, 28, 48] including different image restoration tasks such as deblurring, super-resolution [27], and denoising [4]. However, one major drawback is that transformer models suffer from the heavy computational cost of space and time complexity of $\mathcal{O}(N^2)$ and $\mathcal{O}(N^2C)$, respectively, for N being number of pixels and C being number of features. [17] brings out the concept of using FFT based element-wise product attention, producing favourable space and time complexities of $\mathcal{O}(N)$ and $\mathcal{O}(NC \log(N))$. Despite its efficacy, it really falls out in terms of feature representation, as they lacks high and low frequency feature handling. This is significant for restoration tasks as shown in [9, 29, 51]. The performance of these models gets further limited due to the inability of FT to handle non-stationary signals and showcase spatial-frequency properties.

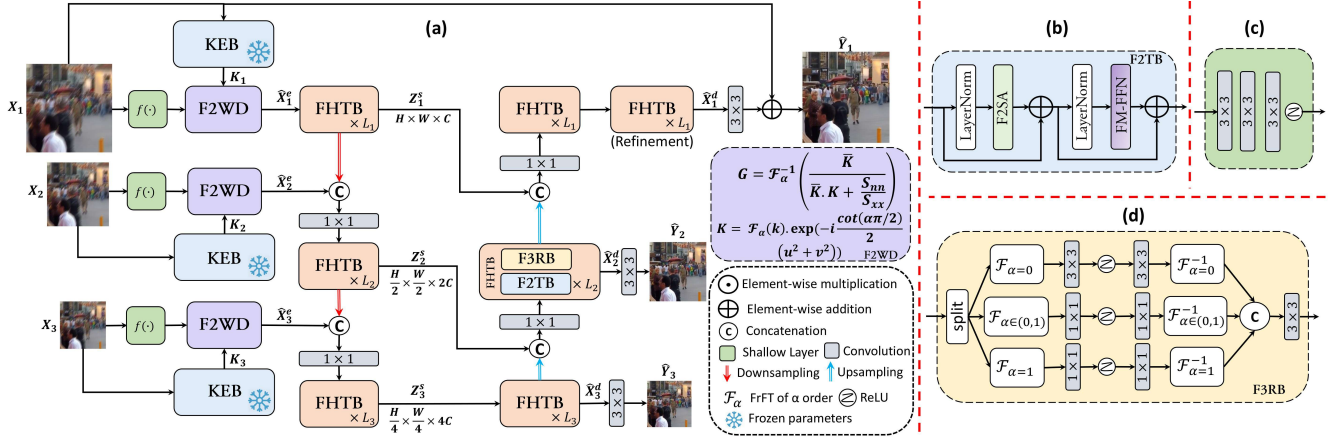


Figure 3. (a) Overall architecture of F2former. Given input \mathbf{X}_p for p -th scale, KEB estimates the blur kernel \mathbf{K}_p . Given \mathbf{X}_p , (c) shallow layers extract features and F2WD refines them by performing deblurring using FRFT based feature Wiener deconvolution. Refined features $\hat{\mathbf{X}}_p^e$ pass through FHTB blocks for efficient image reconstruction. An FHTB consists of a FRFT based (d) feature refinement block, and L_p numbers of (b) F2TBs, which consist of two major modules - self-attention estimation in FRFT domain by F2SA and frequency selective feed-forward operation by FM-FFN.

2.2. Deep Wiener deconvolution and FRFT

Traditionally, image deblurring techniques aim to accurately estimate the blur kernel. Most DL models that learn directly with clean-degraded pairs are limited as they are unable to explicitly use this information. [14] shows that accurate estimation of this blur pattern and incorporation of this information into latent space lead to SOTA performance in benchmark datasets. Previously, [37] demonstrated the effectiveness of learnable kernels in microscopy image restoration by formulating them as regularizer and integrating it in Wiener-Kolmogorov filter. Later, [11, 58] integrated classical Wiener deconvolution along with DL models. They apply Wiener deconvolution in feature space to enhance the semantic information by deblurring them in latent domain. They achieved SOTA performance when the blur kernel is known. However, these models struggle with spatially varying and non-uniform blur as they utilize only FT. Some early methods demonstrated that FRFT based image restoration techniques developed using Wiener deconvolution [21, 50] can handle non-stationary signals as well as time varying characteristics much better, as the FRFT offers a more flexible and adaptive approach in analyzing and filtering such signals compared to FT. Recently, [52] explored the efficacy of using FRFT in DL models achieving superior performance in different image restoration tasks. Inspired by this, in this work, we present an FRFT oriented feature-based Wiener deconvolution, along with a transformer block consisting of FRFT based self-attention and a custom FFN block to effectively work on high and low frequency features resulting in enhanced feature representation while showcasing similar complexity to [17].

3. Methodology

3.1. Preliminary of FRFT

The FRFT is a generalization of the FT with a fractional parameter $\alpha \in [0, 1]$. For a 1-D signal $x(s)$, where s represents a spatial domain, say the FRFT of the signal is $X_\alpha(t_\alpha)$. Then, the α -th order FRFT ($\mathcal{F}_\alpha\{\cdot\}$) and inverse FRFT (IFRFT) ($\mathcal{F}_\alpha^{-1}\{\cdot\}$) are defined as [32],

$$\mathcal{F}_\alpha\{x(s)\}(t_\alpha) = X_\alpha(t_\alpha) = \int_{-\infty}^{\infty} K_\alpha(s, t_\alpha)x(s)ds \quad (2)$$

$$\mathcal{F}_\alpha^{-1}\{X_\alpha(t_\alpha)\}(s) = x(s) = \int_{-\infty}^{\infty} K_{-\alpha}(s, t_\alpha)X_\alpha(t_\alpha)dt_\alpha,$$

where, kernel $K_\alpha(s, t_\alpha)$ is defined as,

$$K_\alpha = \begin{cases} A_\alpha e^{[\pi i (s^2 \cot \theta - 2st_\alpha \csc \theta + t_\alpha^2 \cot \theta)]}, & \theta \neq n\pi, \\ \delta(s - t_\alpha), & \theta = 2n\pi, \\ \delta(s + t_\alpha), & \theta = (2n + 1)\pi, \end{cases} \quad (3)$$

where, $A_\alpha = \sqrt{1 - i \cot \theta}$ with $\theta = \frac{\alpha\pi}{2}$, $i = \sqrt{-1}$ and $n \in \mathbb{N}$. When $\alpha = 1$, equation 2 converges to FT formulation. Another important property of FRFT is its relation with Wigner distribution, which for the signal $x(s)$ is defined as,

$$W_x(s, f) = \int_{-\infty}^{\infty} x(s + \frac{\tau}{2})x^*(s - \frac{\tau}{2})e^{-2\pi i f \tau} d\tau, \quad (4)$$

where f is frequency axis. The $W_x(s, f)$ can be interpreted as the distribution of signal energy in the spatial-frequency domain. As shown in [32], it has direct linkage with FRFT and spatial-frequency plane rotation as,

$$W_{X_\alpha}(s, f) = W_x(s \cos \theta - f \sin \theta, s \sin \theta + f \cos \theta). \quad (5)$$

Therefore, FRFT inherits the properties of the Wigner function resulting in high-resolution spatial-frequency representation. To apply FRFT for images, the discrete version (DFRFT) [33] is defined,

$$\mathbf{F}_{m,n}^\alpha = \sum_{l=0, l \neq N-(N)_2}^N \mathbf{u}_m^l e^{(-i\frac{\alpha\pi}{2}l)} \mathbf{u}_n^l, \quad (6)$$

where, N is the size of the image matrix and $(N)_2$ denotes the parity, and \mathbf{u}^l is l -th eigenvector of the normalized Discrete FT (DFT), i.e., l -th discrete Hermite Gaussian [16]. Equation 6 converges to unitary when $\alpha = 0$ and to normalized DFT matrix when $\alpha = 1$.

3.2. Network architecture

The overall framework of F2former is shown in Figure 3 (a). Here, we employ a U-Net like three-scale ($p = \{1, 2, 3\}$) encoder-decoder architecture. Inspired by previous works [7], we also use multi-input and multi-output strategy across different scales to overcome training difficulty. Input images of reduced sizes are fed into the model and the corresponding predicted images ($\hat{\mathbf{Y}}_p$) are estimated by 3×3 convolution after each scale in the decoder. Therefore, for a blurry image $\mathbf{X}_p \in \mathbb{R}^{\frac{H}{2^{p-1}} \times \frac{W}{2^{p-1}} \times 2^{p-1} C}$ at scale p , a frozen kernel estimation block (KEB) estimates its blur kernel \mathbf{K}_p . The KEB is modelled based on [14] and [49]. More details about KEB are provided in implementation details in Appendix A.3 of supplementary. Given estimated \mathbf{K}_p , and $f(\mathbf{X}_p)$, F2WD performs deblurring at feature level to enhance the low-level feature representations, where $f(\cdot)$ is shallow layer consisting of CNN layers as shown in Figure 3 (c). The refined features $\hat{\mathbf{X}}_p^e$ are passed to the main encoder-decoder model. At each scale of this model, there is an FHTB block consisting of an F3RB layer followed by L_p number of F2TB layers. F3RB is designed inspired by [52] to extract features at different context level by implying FRFT followed by CNN for different α values as shown in Figure 3 (d). However, here we also employ ReLU activations before IFRFT as they refine features by selecting certain frequency components [30]. We also use skip connections between encoder and decoder features to assist in effective gradient flow during training, and implement up-sampling and downsampling via pixel shuffle and unshuffle operations. Next, we discuss the functionality of F2WD and F2TB in detail.

3.2.1 Fractional Feature based Wiener Deconvolution (F2WD)

[11] shows for a set of linear filters, the derivation of the feature-based Wiener deconvolution (FWD) operator is similar to the classical one. Although deep CNN features are non-linear, they are locally linear [22]. There-

fore, [11] estimates the blurry features using deep convolution layers and performs Wiener deconvolution in the feature space. They further demonstrate the advantage of performing the FWD operation in deep feature space instead of image space. Inspired by this, we introduce F2WD to refine the features at the shallow level.

The major issue in [11] is limited performance for non-uniform blur, as for arbitrary spatially varying degradation or nonstationary processes like images, the derived deconvolution operator cannot be realized adequately in Fourier domain due to their time-variant properties. As these properties are more realizable in fractional Fourier domain, we derive the FWD operator (\mathbf{G}) using FRFT [21] as shown in proposition 1.

Proposition 1 Consider \mathbf{K}_p be the estimated blur kernel. Then, for the j -th feature, the FWD operator in the FRFT domain can be estimated as

$$\mathbf{G}_j^p = \frac{(\mathbf{C}\mathbf{F}^\alpha \mathbf{S}_j^{xx} \mathbf{K}_p^H \mathbf{F}^{-\alpha})^H}{\mathbf{F}^\alpha (\mathbf{K}_p \mathbf{S}_j^{xx} \mathbf{K}_p^H + \mathbf{S}_j^{nn}) \mathbf{F}^{-\alpha}}, \quad (7)$$

where, $(\cdot)^H$ is conjugate transpose operation, \mathbf{S}_j^{xx} and \mathbf{S}_j^{nn} is auto-correlation of clean signal and noise content for j -th feature, \mathbf{C} is a diagonal matrix corresponds to chirp multiplication with diagonal elements $\mathbf{C}_{kk} = e^{-ik^2 \cot \theta/2}$.

Detailed proof of the above proposition is provided in the Appendix B of supplementary. Here, we follow [11] to estimate \mathbf{S}_j^{xx} and \mathbf{S}_j^{nn} . Hence, for each scale p , F2WD performs deconvolution using the above derived operator (\mathbf{G}^p) with low level features $f(\mathbf{X}_p)$ such that $\hat{\mathbf{X}}_p^e = \mathbf{G}^p f(\mathbf{X}_p)$ as shown in Figure 3 (a). To show the efficacy of the proposed F2WD, we have presented a comparative feature visualization in the ablation study.

3.2.2 Fractional frequency based transformer block (F2TB)

Each F2TB consists of two important modules, F2SA and FM-FFN as shown in Figure 3 (a).

Fractional Frequency aware Self-Attention (F2SA).

The detail architectural of F2SA are shown in Figure 4 (a). The major issue with transformers is their computational overhead in self-attention (SA) layer, as time and space complexities increase quadratically ($\mathcal{O}(N^2)$). [17] introduces query-key Hadamard product attention in Fourier domain as an alternate resulting in a version with $\mathcal{O}(N \log N)$ complexity. Here, we present a similar attention mechanism, but in the FRFT domain with the awareness of important spatial-frequency components.

For an input $\mathbf{X}_{in}^{SA} \in \mathbb{R}^{H \times W \times C}$, F2TB estimates query (\mathbf{Q}), key (\mathbf{K}) and value (\mathbf{V}) matrix by linear projections, i.e., $\mathbf{Q} = W_q \mathbf{X}_{in}^{SA}$, $\mathbf{K} = W_k \mathbf{X}_{in}^{SA}$, and $\mathbf{V} = W_v \mathbf{X}_{in}^{SA}$, where, $W_{(\cdot)}$ corresponds to 1×1 convolution followed by

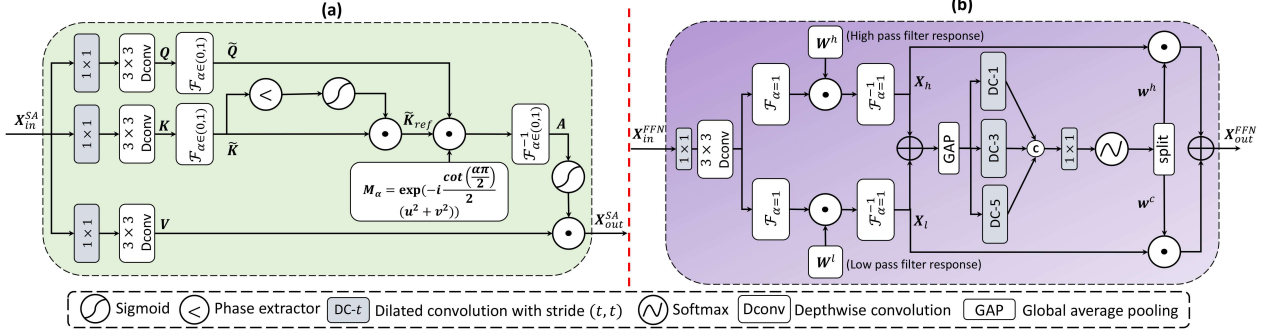


Figure 4. Architecture of F2TB layer. Overview of (a) Fractional Fourier aware Self-Attention (F2SA) and (b) Frequency division multiplexing based Feed Forward Network (FM-FFN)

3×3 depth-wise convolution. During estimating Hadamard-product attention, we follow the convolution theorem associated with FRFT [55] as follows

$$\mathcal{F}_\alpha\{x(s) * y(s)\}(t_\alpha) = e^{-it_\alpha^2 \cot \theta/2} X(t_\alpha) Y(t_\alpha) \quad (8)$$

Hence, during element-wise attention estimation, we also have to consider the chirp equivalent matrix $M_\alpha = \mathbf{m}_H \mathbf{m}_W^T$, where $\mathbf{m}_N = [e^{-i.1^2. \cot \theta/2} \quad e^{-i.2^2. \cot \theta/2} \quad \dots \quad e^{-i.N^2. \cot \theta/2}]^T$.

For attention estimation, the projected Q and K in FRFT domain can be written as $\tilde{Q} = \mathbf{F}^\alpha Q$ and $\tilde{K} = \mathbf{F}^\alpha K$. Instead of directly using \tilde{K} , we refine it based on important frequency components. As the phase of FRFT consists of relevant spatial-frequency information [38], we use that as a modulator to update \tilde{K} . As illustrated in Figure 4 (a), the refined key in the FRFT domain is estimated as

$$\tilde{K}_{ref} = \sigma(\arg(\tilde{K})) \odot \tilde{K}, \quad (9)$$

where $\arg(\cdot)$ represents phase component, \odot is Hadamard product, and $\sigma(\cdot)$ is Sigmoid operation. Then, the attention can be estimated as

$$\mathbf{A} = \mathbf{F}^{-\alpha} (M_\alpha \odot (\tilde{Q} \odot \tilde{K}_{ref}^H)^H). \quad (10)$$

Finally, the output of F2SA is estimated as

$$\mathbf{X}_{out}^{SA} = \mathbf{X}_{in}^{SA} + conv(\sigma(\mathbf{A}) \odot \mathbf{V}), \quad (11)$$

where, $conv(\cdot)$ is 1×1 CNN operation. For computing attention, we divide the number of channels into heads to learn them parallelly similar to conventional multi-head SA [12]. For the optimal choice of α in F3RB, F2WD and F2SA, we use it as a learnable parameter as suggested by [18].

Frequency division Multiplexing based FFN (FM-FFN). We design FFN to further refine the features from F2SA based on selective frequency components as shown in Figure 4 (b). Given input $\mathbf{X}_{in}^{FFN} \in \mathbb{R}^{H \times W \times C}$, we reproject them using W_{FFN} and apply high and low pass

filter operation in FFT domain to divide the features into different frequency components. Hence, the estimated high (\mathbf{X}_h) and low (\mathbf{X}_l) frequency components can be expressed as

$$\begin{aligned} \mathbf{X}_h &= \mathbf{F}^\alpha (\mathbf{W}^h \odot (W_{FFN} \mathbf{X}_{in}^{FFN})) \mathbf{F}^{-\alpha}, \\ \mathbf{X}_l &= \mathbf{F}^\alpha (\mathbf{W}^l \odot (W_{FFN} \mathbf{X}_{in}^{FFN})) \mathbf{F}^{-\alpha}, \end{aligned} \quad (12)$$

where, we set $\alpha = 1$ for operation in FT domain, and \mathbf{W}^h and \mathbf{W}^l correspond to high and low pass filter response. Here, we prefer FT as it is easy to separate different frequency components in a frequency only representation. The \mathbf{W}^l is estimated using the cosine bell function (CBF) defined as follows,

$$\mathbf{W}_{j,k}^l = 0.5 \left(1 + \cos \left(\frac{\pi \sqrt{j^2 + k^2}}{\lambda} \right) \right), \quad (13)$$

where λ is learnable low-pass cut-off frequency. From this, the high pass response is estimated as $\mathbf{W}^h = \mathbf{I} - \mathbf{W}^l$ with \mathbf{I} being the identity matrix. The main advantage of CBF is its smooth transition, resulting in fewer ringing artefacts during inverse operation. We validate this with our ablation study.

To emphasize important frequency components, we leverage frequency multiplexing operation based on [25]. Specifically, to get channel-wise weights related to significant frequency elements, we perform $\mathbf{Z} = GAP(\mathbf{X}_h + \mathbf{X}_l)$ such that $\mathbf{Z} \in \mathbb{R}^{1 \times 1 \times C}$, where $GAP(\cdot)$ is global average pooling, followed by 3×3 CNN with different dilation rates of 3, 5, and 7 as shown in Figure 4 (b) to extract features at different receptive fields. They are later concatenated and passed to 1×1 CNN and Softmax activation, formulated as, $(\mathbf{w}^h \oplus \mathbf{w}^l)_c = \frac{e^{(W_D \mathbf{Z})_c}}{\sum_j e^{(W_D \mathbf{Z})_j}}$, where W_D corresponds to all intermediate CNN operation, \mathbf{w}^h and \mathbf{w}^l are channel-wise attention weights for low and high frequency components, and \oplus represents concatenation. The final weights can be obtained by split operation. Therefore, the final output of FM-FFN can be written as,

$$\mathbf{X}_{out}^{FFN} = \mathbf{X}_{in}^{FFN} + conv((\mathbf{w}^l \odot \mathbf{X}_l) + (\mathbf{w}^h \odot \mathbf{X}_h)). \quad (14)$$

Table 1. Quantitative comparison of SOTA methods on GoPro, HIDE, RealBlur-R, and RealBlur-J datasets for setting \mathcal{A} . The first and second best results are in bold and underlined. Inference time is based on testing of 256×256 image patch.

Method	GoPro		HIDE		RealBlur-R		RealBlur-J		Avg. Runtime (s)	Parameters (M)
	PSNR \uparrow	SSIM \uparrow								
DMPHN [56]	31.20	0.940	29.09	0.924	35.70	0.948	28.42	0.860	0.21	21.7
DBGAN [57]	31.10	0.942	28.94	0.915	35.78	0.909	24.93	0.745	0.04	60.9
MT-RNN [36]	31.15	0.945	29.15	0.918	35.79	0.951	28.44	0.862	-	-
MPRNet [54]	32.66	0.959	30.96	0.939	35.99	0.952	28.70	0.873	0.09	20.1
MIMO-UNet+ [8]	32.45	0.957	29.99	0.930	35.54	0.947	27.63	0.837	-	16.1
Uformer [44]	33.06	0.967	30.90	0.953	36.19	0.956	29.09	0.886	0.07	50.9
NAFNet64 [6]	33.69	0.967	31.32	0.943	35.84	0.952	29.94	0.854	0.04	67.9
Stripformer [43]	33.30	0.966	31.16	0.950	-	-	-	-	0.04	19.7
Restormer [53]	32.92	0.961	31.22	0.942	36.19	0.957	28.96	0.879	0.08	26.1
DeepRFT+ [30]	33.52	0.965	31.66	0.946	36.11	0.955	28.90	0.881	0.09	23.0
FFTformer [17]	34.21	0.968	31.62	0.946	-	-	-	-	0.13	16.6
UFPNet [14]	34.06	0.968	31.74	0.947	36.25	0.953	29.87	0.884	-	80.3
MRLPFNet [10]	34.01	0.968	31.63	0.947	-	-	-	-	0.863	20.6
AdaRevD [46]	<u>34.64</u>	<u>0.972</u>	<u>32.37</u>	<u>0.953</u>	<u>36.60</u>	<u>0.958</u>	<u>30.14</u>	<u>0.895</u>	-	-
F2former-S (ours)	34.77	0.963	33.07	0.958	36.64	0.959	30.88	0.907	0.15	9.29
F2former-B (ours)	35.17	0.970	33.43	0.966	36.84	0.961	31.25	0.918	0.22	18.3
F2former-L (ours)	35.22	0.975	33.48	0.971	36.88	0.967	31.34	0.920	0.27	26.2

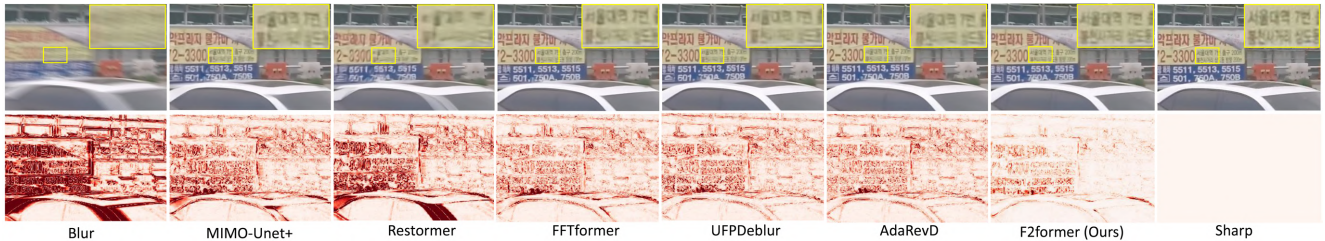


Figure 5. Visual illustration on the GoPro test dataset. The first row shows blurred image, predicted images of various methods, and GT sharp image. The second row shows the residual of the respective blurred image and predicted sharp images with GT.

Due to page limitations, we discuss the objective functions and implementation details to train our network in Appendix A.1 of supplementary.

4. Experimental Results

4.1. Dataset and Experimental Setup

We investigate the effectiveness of the proposed method for both motion blur and spatially varying non-uniform blur by evaluating five different commonly used benchmark datasets: GoPro [31], HIDE [41], RealBlur-R and RealBlur-J [39], and Dual-Pixel Defocus Deblurring (DPDD) [1]. For detailed analysis, we introduce three F2former variants, F2former-S (Small), F2former-B (Base), and F2former-L (Large) based on feature channels C and number of Transformer blocks in FHTB, $L = \{L_1, L_2, L_3\}$ as shown in Figure 3 (a). For all three variants, we take $C = 48$. For base model, we select $L = \{2, 4, 8\}$, while for large and small model we take $L = \{4, 8, 12\}$ and $L = \{2, 2, 2\}$, respectively. The details about other parameter settings are given in the Appendix A.2 of supplementary.

4.2. Evaluation of trained model on GoPro

Table 1 shows the quantitative performance of F2former trained on the GoPro dataset and compares it with other SOTA methods on the test set of GoPro, HIDE, RealBlur-J and RealBlur-R datasets. We define this set-up as setting \mathcal{A} . As shown, F2former outperforms other methods in terms of both PSNR and SSIM for all four datasets. Compared to the second best, our base model achieves 0.53 dB gain in PSNR for the GoPro test dataset, while for the HIDE and RealBlur-J datasets, the gain is more than 1 dB. This can be validated from the visual comparison as shown in Figure 5. The superior performance is attributed to the improved feature domain deblurring of F2WD and the representation power of FRFT-based transformer block.

Table 1 shows the parameter dependency and execution time of F2former. Since FRFT involves chirp multiplication and does not have an optimized implementation like FFT, the average runtime of F2former is slightly higher but competitive against other SOTA methods. In terms of parameters, the small model has 50% less parameters with a notable performance drop, while the large model has marginal

Table 2. Defocus deblurring comparisons on the DPDD testset (containing 37 indoor and 39 outdoor scenes) for setting \mathcal{B} . **S**: single-image defocus deblurring. **D**: dual-pixel defocus deblurring.

Method	Indoor Scenes				Outdoor Scenes				Combined			
	PSNR \uparrow	SSIM \uparrow	MAE \downarrow	LPIPS \downarrow	PSNR \uparrow	SSIM \uparrow	MAE \downarrow	LPIPS \downarrow	PSNR \uparrow	SSIM \uparrow	MAE \downarrow	LPIPS \downarrow
DMENet _S [23]	25.50	0.788	0.038	0.298	21.43	0.644	0.063	0.397	23.41	0.714	0.051	0.349
KPAC _S [42]	27.97	0.852	0.026	0.182	22.62	0.701	0.053	0.269	25.22	0.774	0.040	0.227
IFAN _S [24]	28.11	0.861	0.026	0.179	22.76	0.720	0.052	0.254	25.37	0.789	0.039	0.217
SFNet _S [9]	29.16	0.878	0.023	0.168	23.45	0.747	0.049	0.244	26.33	0.811	0.037	0.207
Restormer _S [53]	28.87	0.882	0.025	0.145	23.24	0.743	0.050	0.209	25.98	0.811	0.038	0.178
GRL-B _S [26]	<u>29.06</u>	<u>0.886</u>	<u>0.024</u>	<u>0.139</u>	<u>23.45</u>	<u>0.761</u>	<u>0.049</u>	<u>0.196</u>	<u>26.18</u>	<u>0.822</u>	<u>0.037</u>	<u>0.168</u>
F2former _S (ours)	31.18	0.905	0.011	0.109	26.60	0.814	0.032	0.134	28.89	0.865	0.022	0.121
RD _D [2]	28.10	0.843	0.027	0.210	22.82	0.704	0.053	0.298	25.39	0.772	0.040	0.255
Uformer _D [44]	28.23	0.859	0.026	0.199	22.95	0.728	0.051	0.285	25.59	0.795	0.039	0.243
IFAN _D [24]	28.66	0.870	0.025	0.172	23.46	0.743	0.049	0.254	25.99	0.804	0.037	0.207
Restormer _D [53]	29.48	0.895	0.023	0.134	23.97	0.773	0.047	0.175	26.66	0.833	0.035	0.155
LAKDNet _D [40]	29.76	0.893	0.023	<u>0.109</u>	<u>24.42</u>	0.765	<u>0.045</u>	<u>0.142</u>	27.02	0.829	0.034	0.140
GRL-B _D [26]	29.83	<u>0.903</u>	<u>0.022</u>	0.114	24.39	<u>0.795</u>	<u>0.045</u>	0.150	<u>27.04</u>	<u>0.847</u>	<u>0.034</u>	<u>0.133</u>
F2former _D (ours)	32.06	0.920	0.015	0.097	27.19	0.825	0.028	0.119	29.63	0.875	0.022	0.108

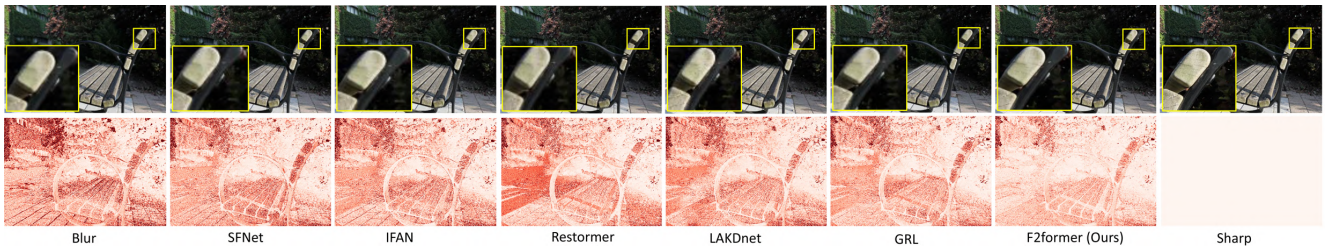


Figure 6. Visual illustration on the dual pixel DPDD test dataset. First row shows blurred images, predicted images of various methods, and GT sharp images. Second row shows the residual of the blurred image and predicted sharp images with GT.

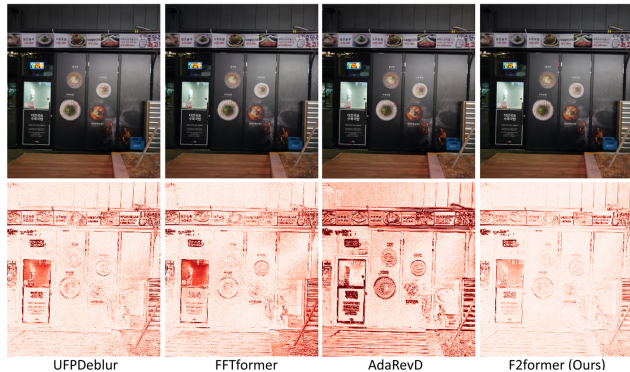


Figure 7. Visual illustration on RealBlur-J test dataset

improvement with 42% more parameters. Hence, the rest of the experiments are carried out with the base model.

4.3. Evaluation of trained model on DPDD

Table 2 shows the performance comparison for different scenarios of defocus blur on the DPDD test dataset. We define this set-up as setting \mathcal{B} . In this case, the F2former is trained separately for both single and dual-pixel defocus deblurring tasks. Clearly, F2former has significant performance gains for all scene categories due to its ability to

Table 3. Comparison on RealBlur for setting \mathcal{C} .

Method	RealBlur-R		RealBlur-J		Average	
	PSNR \uparrow	SSIM \uparrow	PSNR \uparrow	SSIM \uparrow	PSNR \uparrow	SSIM \uparrow
DeblurGAN-v2	36.44	0.935	29.69	0.870	33.07	0.903
SRN	38.65	0.965	31.38	0.909	35.02	0.937
MPRNet	39.31	0.972	31.76	0.922	35.54	0.947
MAXIM	39.45	0.962	32.84	0.935	36.15	0.949
Stripformer	39.84	0.974	32.48	0.929	36.16	0.952
DeepRFT+	40.01	0.973	32.63	0.933	36.32	0.953
FFTformer	40.11	0.975	32.62	0.933	36.37	0.954
UFPNet	40.61	0.974	33.35	0.934	36.98	0.954
MRLPFNet	40.92	0.975	33.19	0.936	37.06	0.956
AdaRevD	<u>41.09</u>	<u>0.978</u>	<u>33.84</u>	<u>0.943</u>	<u>37.47</u>	<u>0.961</u>
F2former	41.62	0.982	34.53	0.955	38.08	0.969

handle spatially varying blur. Specifically, for both single and dual pixel defocus deblurring cases, F2former achieves more than 2 dB performance gain over GRL [26]. This also can be validated from Figure 6, where, the F2former removes the non-uniform blur most effectively.

4.4. Evaluation of trained model on RealBlur

We train our model on RealBlur-J and RealBlur-R separately. We define this set-up as setting \mathcal{C} for which table 3 shows the performance comparison on respective test datasets. F2former has the best performance with more than 0.5-0.6 dB gain in PSNR compared to the second best.

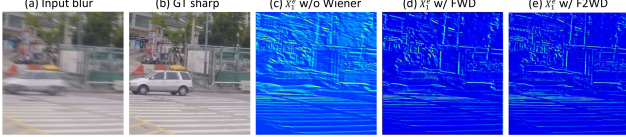


Figure 8. Visualization of shallow features to show the effect of F2WD (better visualized at 200%)



Figure 9. Effectiveness of FRFT-based self-attention on predicted image, compared to FFT based self-attention

This also can be visualized from Figure 7, where F2former predicts sharper images compared to other SOTA methods. More visual results are provided in the supplementary.

5. Analysis and Discussion

We discuss the effect of each of the proposed module. For the related ablation studies, all experiments are performed with the base model trained with the GoPro dataset.

Effect of F2WD. The major contribution of F2WD is to refine shallow-level features by performing fractional Wiener deconvolution in feature space to produce sharper features which make the image reconstruction task efficient. Figure 8 supports the observation that applying Wiener deconvolution results in sharper features during training of F2former. Compared to feature-based Wiener deconvolution (FWD), the feature enhancement in the case of F2WD is sharper which also justifies our results in Table 4. Introducing F2WD, there is 0.4 dB and 0.14 dB improvement in PSNR compared to baseline (no Wiener deconvolution) and the FWD case. To further verify, we retrain the Restormer with FWD and F2WD applied to shallow features before the transformer blocks. As shown in Table 4, we see similar improvement compared to baseline Restormer performance.

Effect of F2SA. We implement FRFT from [18] which has a complexity of $\mathcal{O}(N \log N)$, implemented based on [32]. Hence, similar to FFTformer, F2SA has a space and time complexity of $\mathcal{O}(N)$ and $\mathcal{O}(NC \log N)$, which is lower compared to $\mathcal{O}(N^2)$ and $\mathcal{O}(N^2C)$ in conventional SA. Besides computational efficiency, as F2SA is based on FRFT, the attention computation occurs in the spatial-frequency domain resulting in capturing relevant information in both spatial and frequency domain. This helps in more effective deblurring as shown in Figure 9 where we replace FRFT with FFT operation during self-attention (SA) estimation. We also validate the effectiveness of phase modulation (PM) during SA computation by retraining FFT-

Table 4. Quantitative evaluation of each proposed component for different models

Models	w/ FWD	w/ F2WD	w/ PM in SA	w/ FM-FFN	w/ DFFN	PSNR/SSIM
Restormer	✓	✗	✗	✗	✗	33.48/0.964
	✗	✓	✗	✗	✗	33.63/0.969
FFTformer	✗	✗	✓	✗	✓	34.38/0.968
	✗	✗	✓	✓	✗	34.52/0.969
F2former	✗	✗	✓	✗	✓	34.53/0.961
	✗	✗	✓	✓	✗	34.76/0.963
	✓	✗	✓	✓	✗	35.03/0.968
	✗	✓	✓	✓	✗	35.17/0.970

former with this module. As shown in Table 4, it improves its baseline performance by 0.17 dB in PSNR.

Effect of FM-FFN. We introduce frequency division multiplexing (FM) in the FFN block to emphasize significant frequency components. For baseline comparison, we replace our FM-FFN with discriminative frequency domain based FFN (DFFN) from [17] in our framework. As shown in Table 4, there is a 0.22 dB PSNR reduction compared to using FM-FFN. For further validation, we include FM-FFN in FFTformer to retrain the model in the presence of PM in SA and notice an increase in performance by 0.14 dB PSNR. Further ablation studies related to choosing a cosine bell as a filter as well as visualization of its learnable threshold, the low and high pass response and also the α parameter for FRFT are carried out in Appendix C of supp.

6. Conclusion

In this work, we propose F2former, an effective deblurring approach based on the Fractional Fourier Transform (FRFT). As evident from the experiments, our Fractional-Fourier Transform (FRFT) based method achieves impressive deblurring even with spatially varying blur which is usually not handled well by spatial-only or Fourier-only methods. The main performance of our method comes from specially designed Fractional Feature based Wiener Deconvolution block and the Fractional Frequency aware Transformer block, which work with relevant spatio-spectral features for effective deblurring. The transformer layer extracts and utilizes relevant frequency components via a phase modulated SA and a frequency division multiplexing based feed-forward network. Experiments on different benchmark datasets for both motion and defocus blur show that our method performs favourably against other SOTA methods.

Limitation: F2former relies on the accuracy of estimated blur kernel by KEB, a separate trained model. Here, we also assume the CNN operations to be locally linear to apply F2WD which may result in erroneous feature maps occasionally. In future, we will investigate the blur kernel estimation in feature space only and incorporate it with the main deblurring network to train in an end-to-end manner for efficient image deblurring. We will also validate the effectiveness of FRFT for other image restoration tasks like super-resolution, denoising and dehazing.

References

- [1] Abdullah Abuolaim and Michael S Brown. Defocus deblurring using dual-pixel data. In *European Conference on Computer Vision*, pages 111–126. Springer, 2020. 6
- [2] Abdullah Abuolaim, Mauricio Delbracio, Damien Kelly, Michael Brown, and Peyman Milanfar. Learning to reduce defocus blur by realistically modeling dual-pixel data. In *Proc. ICCV*, pages 2269–2278, 10 2021. 7
- [3] Nicolas Carion, Francisco Massa, Gabriel Synnaeve, Nicolas Usunier, Alexander Kirillov, and Sergey Zagoruyko. End-to-end object detection with transformer. In *Proceedings of the European Conference on Computer Vision (ECCV)*, 2020. 2
- [4] Hanting Chen, Yunhe Wang, Tianyu Guo, Chang Xu, Yiping Deng, Zhenhua Liu, Siwei Ma, Chunjing Xu, Chao Xu, and Wen Gao. Pre-trained image processing transformer. In *Proceedings of the IEEE/CVF Conference on Computer Vision and Pattern Recognition (CVPR)*, 2021. 2
- [5] Liangyu Chen, Xiaojie Chu, Xiangyu Zhang, and Jian Sun. Simple baselines for image restoration. In *Proceedings of the European Conference on Computer Vision (ECCV)*, 2022. 2
- [6] Liangyu Chen, Xiaojie Chu, Xiangyu Zhang, and Jian Sun. Simple baselines for image restoration. *arXiv preprint arXiv:2204.04676*, 2022. 2, 6, 11
- [7] Sung-Jin Cho, Seo-Won Ji, Jun-Pyo Hong, Seung-Won Jung, and Sung-Jea Ko. Rethinking coarse-to-fine approach in single image deblurring. In *2021 IEEE/CVF International Conference on Computer Vision (ICCV)*, pages 4621–4630, 2021. 4
- [8] Sung-Jin Cho, Seo-Won Ji, Jun-Pyo Hong, Seung-Won Jung, and Sung-Jea Ko. Rethinking coarse-to-fine approach in single image deblurring. In *Proc. ICCV*, pages 4621–4630, 10 2021. 6
- [9] Yuning Cui, Yi Tao, Zhenshan Bing, Wenqi Ren, Xinwei Gao, Xiaochun Cao, Kai Huang, and Alois Knoll. Selective frequency network for image restoration. In *The Eleventh International Conference on Learning Representations*, 2023. 2, 7, 11
- [10] Jiangxin Dong, Jinshan Pan, Zhongbao Yang, and Jinhui Tang. Multi-scale residual low-pass filter network for image deblurring. In *Proc. ICCV*, pages 12311–12320, 10 2023. 6
- [11] Jiangxin Dong, Stefan Roth, and Bernt Schiele. Deep wiener deconvolution: Wiener meets deep learning for image deblurring. *Advances in Neural Information Processing Systems*, 33:1048–1059, 2020. 3, 4
- [12] Alexey Dosovitskiy, Lucas Beyer, Alexander Kolesnikov, Dirk Weissenborn, Xiaohua Zhai, Thomas Unterthiner, Mostafa Dehghani, Matthias Minderer, Georg Heigold, Sylvain Gelly, et al. An image is worth 16x16 words: Transformers for image recognition at scale. In *International Conference on Learning Representations (ICLR)*, 2021. 5
- [13] Lutfiye Durak and Orhan Arikan. Short-time fourier transform: two fundamental properties and an optimal implementation. *IEEE Transactions on Signal Processing*, 51(5):1231–1242, 2003. 2
- [14] Zhenxuan Fang, Fangfang Wu, Weisheng Dong, Xin Li, Jinjian Wu, and Guangming Shi. Self-supervised non-uniform kernel estimation with flow-based motion prior for blind image deblurring. In *Proceedings of the IEEE/CVF Conference on Computer Vision and Pattern Recognition*, pages 18105–18114, 2023. 1, 3, 4, 6, 11
- [15] Marie Farge. Wavelet transforms and their applications to turbulence. *Annual Review of Fluid Mechanics*, 24(1):395–458, 1992. 2
- [16] Loukas Grafakos. Classical fourier analysis. 2010. 4
- [17] Lingshun Kong, Jiangxin Dong, Jianjun Ge, Mingqiang Li, and Jinshan Pan. Efficient frequency domain-based transformers for high-quality image deblurring. In *Proceedings of the IEEE Conference on Computer Vision and Pattern Recognition (CVPR)*, 2023. 2, 3, 4, 6, 8, 11
- [18] Emirhan Koç, Tuna Alikashiöglu, Arda Can Aras, and Aykut Koç. Trainable fractional fourier transform. *IEEE Signal Processing Letters*, 31:751–755, 2024. 5, 8
- [19] D. Krishnan and R. Fergus. Fast image deconvolution using hyper-laplacian priors. In *Advances in Neural Information Processing Systems (NIPS)*, pages 1033–1041, 2009. 1
- [20] D. Kundur and D. Hatzinakos. Blind image deconvolution. *IEEE Signal Processing Magazine*, 13(3):43–64, 1996. 1
- [21] M.A. Kutay, H.M. Ozaktas, L. Onural, and O. Arikan. Optimal filtering in fractional fourier domains. In *1995 International Conference on Acoustics, Speech, and Signal Processing*, volume 2, pages 937–940 vol.2, 1995. 3, 4
- [22] G.-H. Lee, D. Alvarez-Melis, and T. S. Jaakkola. Towards robust, locally linear deep networks. In *International Conference on Learning Representations (ICLR)*, 2019. 4
- [23] Junyong Lee, Sungkil Lee, Sunghyun Cho, and Seungyong Lee. Deep defocus map estimation using domain adaptation. In *Proceedings of the IEEE Conference on Computer Vision and Pattern Recognition (CVPR)*, 2019. 7
- [24] Junyong Lee, Hyeongseok Son, Jaesung Rim, Sunghyun Cho, and Seungyong Lee. Iterative filter adaptive network for single image defocus deblurring. In *2021 IEEE/CVF Conference on Computer Vision and Pattern Recognition (CVPR)*, pages 2034–2042, 2021. 7
- [25] Xiang Li, Wenhai Wang, Xiaolin Hu, and Jian Yang. Selective kernel networks. In *2019 IEEE/CVF Conference on Computer Vision and Pattern Recognition (CVPR)*, pages 510–519, 2019. 5
- [26] Yawei Li, Yuchen Fan, Xiaoyu Xiang, Denis Demandolx, Rakesh Ranjan, Radu Timofte, and Luc Van Gool. Efficient and explicit modelling of image hierarchies for image restoration. In *2023 IEEE/CVF Conference on Computer Vision and Pattern Recognition (CVPR)*, pages 18278–18289, 2023. 7
- [27] Jingyun Liang, Jiezhong Cao, Guolei Sun, Kai Zhang, Luc Van Gool, and Radu Timofte. Swinir: Image restoration using swin transformer. In *Proceedings of the IEEE/CVF International Conference on Computer Vision (ICCV) Workshops*, 2021. 2
- [28] Ze Liu, Yutong Lin, Yue Cao, Han Hu, Yixuan Wei, Zheng Zhang, Stephen Lin, and Baining Guo. Swin transformer: Hierarchical vision transformer using shifted windows. In *Proceedings of the IEEE/CVF International Conference on Computer Vision (ICCV)*, 2021. 2

- [29] Xintian Mao, Yiming Liu, Wei lei Shen, Qingli Li, and Yan Wang. Deep residual fourier transformation for single image deblurring. *ArXiv*, abs/2111.11745, 2021. 2
- [30] Xintian Mao, Yiming Liu, Fengze Liu, Qingli Li, Wei Shen, and Yan Wang. Intriguing findings of frequency selection for image deblurring. In *Proceedings of the 37th AAAI Conference on Artificial Intelligence*, 2023. 4, 6
- [31] Seungjun Nah, Tae Hyun Kim, and Kyoung Mu Lee. Deep multi-scale convolutional neural network for dynamic scene deblurring. In *The IEEE Conference on Computer Vision and Pattern Recognition (CVPR)*, July 2017. 6
- [32] H.M. Ozaktas, O. Arikan, M.A. Kutay, and G. Bozdatg. Digital computation of the fractional fourier transform. *IEEE Transactions on Signal Processing*, 44(9):2141–2150, 1996. 3, 8
- [33] Haldun M. Ozaktas, Zeev Zalevsky, and M. Alper Kutay. *The Fractional Fourier Transform: With Applications in Optics and Signal Processing*. Wiley, New York, NY, USA, 2001. 4
- [34] J. Pan, Z. Lin, Z. Su, and M.-H. Yang. Robust kernel estimation with outliers handling for image deblurring. In *Proceedings of the IEEE Conference on Computer Vision and Pattern Recognition (CVPR)*, pages 2800–2808, 2016. 1
- [35] Liyuan Pan, Richard Hartley, Miaomiao Liu, and Yuchao Dai. Phase-only image based kernel estimation for single image blind deblurring. In *2019 IEEE/CVF Conference on Computer Vision and Pattern Recognition (CVPR)*, pages 6027–6036, 2019. 1
- [36] Dongwon Park, Dong Kang, Jisoo Kim, and Se Young Chun. Multi-temporal recurrent neural networks for progressive non-uniform single image deblurring with incremental temporal training. In *Proc. ECCV*, pages 327–343, 11 2020. 6
- [37] Valeriya Pronina, Filippos Kokkinos, Dmitry V. Dylov, and Stamatios Lefkimmiatis. Microscopy image restoration with deep wiener-kolmogorov filters. In *Computer Vision – ECCV 2020: 16th European Conference, Glasgow, UK, August 23–28, 2020, Proceedings*, page 185–201, Berlin, Heidelberg, 2020. Springer-Verlag. 1, 3
- [38] Mariia Protsenko and Elena Pavelyeva. Fractional fourier transform phase for image matching. pages 688–697, 01 2022. 5
- [39] Jaesung Rim, Haeyun Lee, Jucheol Won, and Sunghyun Cho. Real-world blur dataset for learning and benchmarking deblurring algorithms. In *Proceedings of the European Conference on Computer Vision (ECCV)*, 2020. 6
- [40] Lingyan Ruan, Mojtaba Bemana, Hans peter Seidel, Karol Myszkowski, and Bin Chen. Revisiting image deblurring with an efficient convnet, 2023. 7
- [41] Ziyi Shen, Wenguan Wang, Jianbing Shen, Haibin Ling, Tingfa Xu, and Ling Shao. Human-aware motion deblurring. In *IEEE International Conference on Computer Vision*, 2019. 6
- [42] Hyeongseok Son, Junyong Lee, Sunghyun Cho, and Seungyong Lee. Single image defocus deblurring using kernel-sharing parallel atrous convolutions. In *Proc. ICCV*, 2021. 7
- [43] Fu-Jen Tsai, Yan-Tsung Peng, Yen-Yu Lin, Chung-Chi Tsai, and Chia-Wen Lin. Stripformer: Strip transformer for fast image deblurring. In *Proceedings of the European Conference on Computer Vision (ECCV)*, 2022. 2, 6
- [44] Zhendong Wang, Xiaodong Cun, Jianmin Bao, and Jianzhuang Liu. Uformer: A general u-shaped transformer for image restoration. In *Proceedings of the IEEE Conference on Computer Vision and Pattern Recognition (CVPR)*, 2022. 2, 6, 7
- [45] N. Wiener. *Extrapolation, Interpolation, and Smoothing of Stationary Time Series: With Engineering Applications*, volume 113. MIT Press, 1949. 1
- [46] Qingli Li Xintian Mao and Yan Wang. Adarevd: Adaptive patch exiting reversible decoder pushes the limit of image deblurring. In *Proc. CVPR*, 2024. 6, 11
- [47] L. Xu and J. Jia. Two-phase kernel estimation for robust motion deblurring. In *Proceedings of the European Conference on Computer Vision (ECCV)*, volume 1, pages 157–170, 2010. 1
- [48] Lian Xu, Wanli Ouyang, Mohammed Bennamoun, Farid Boussaid, and Dan Xu. Multi-class token transformer for weakly supervised semantic segmentation. In *Proceedings of the IEEE/CVF Conference on Computer Vision and Pattern Recognition (CVPR)*, 2022. 2
- [49] Xiangyu Xu, Jinshan Pan, Yu-Jin Zhang, and Ming-Hsuan Yang. Motion blur kernel estimation via deep learning. *IEEE Transactions on Image Processing*, 27(1):194–205, 2018. 4, 11, 12
- [50] Peiming Yan, Yulong Mo, and Hong Liu. Image restoration based on the discrete fraction fourier transform. *Proceedings of SPIE - The International Society for Optical Engineering*, 09 2001. 3
- [51] Hao-Hsiang Yang, Chao-Han Huck Yang, and Yi-Chang James Tsai. Y-net: Multi-scale feature aggregation network with wavelet structure similarity loss function for single image dehazing. In *ICASSP 2020 - 2020 IEEE International Conference on Acoustics, Speech and Signal Processing (ICASSP)*, pages 2628–2632. IEEE, 2020. 2
- [52] Hu Yu, Jie Huang, Lingzhi Li, Man Zhou, and Feng Zhao. Deep fractional fourier transform. In *Proceedings of the 37th International Conference on Neural Information Processing Systems, NIPS '23*, Red Hook, NY, USA, 2023. Curran Associates Inc. 3, 4, 13
- [53] Syed Waqas Zamir, Aditya Arora, Salman Khan, Munawar Hayat, Fahad Shahbaz Khan, and Ming-Hsuan Yang. Restormer: Efficient transformer for high-resolution image restoration. In *CVPR*, 2022. 2, 6, 7
- [54] Syed Waqas Zamir, Aditya Arora, Salman Khan, Munawar Hayat, Fahad Shahbaz Khan, Ming-Hsuan Yang, and Ling Shao. Multi-stage progressive image restoration. In *Proceedings of the IEEE Conference on Computer Vision and Pattern Recognition (CVPR)*, 2021. 2, 6
- [55] A.I. Zayed. A convolution and product theorem for the fractional fourier transform. *IEEE Signal Processing Letters*, 5(4):101–103, 1998. 5
- [56] Hongguang Zhang, Yuchao Dai, Hongdong Li, and Piotr Koniusz. Deep stacked hierarchical multi-patch network for image deblurring. In *The IEEE Conference on Computer Vision and Pattern Recognition (CVPR)*, June 2019. 6

- [57] Kaihao Zhang, Wenhan Luo, Yiran Zhong, Lin Ma, Bjorn Stenger, Wei Liu, and Hongdong Li. Deblurring by realistic blurring. In *Proceedings of the IEEE/CVF Conference on Computer Vision and Pattern Recognition*, pages 2737–2746, 2020. 6
- [58] Zhihong Zhang, Yuxiao Cheng, Jinli Suo, Liheng Bian, and Qionghai Dai. Infwide: Image and feature space wiener deconvolution network for non-blind image deblurring in low-light conditions. *IEEE Transactions on Image Processing*, 32:1390–1402, 2023. 3

7. Supplementary

A. Implementation details

A.1. Loss function

For training F2former, we adopt L1 loss in both spatial and FFT domain similar to [9, 46]. We also include L1 loss in FRFT domain to ensure intactness of the spatial-frequency information. Hence, the overall objective function to optimize our model is defined as,

$$\mathcal{L}_{total} = \mathcal{L}_s + \lambda_{t_1} \mathcal{L}_{t_1} + \lambda_{t_\alpha} \mathcal{L}_{t_\alpha}, \quad (15)$$

where, \mathcal{L}_s , \mathcal{L}_{t_1} , and \mathcal{L}_{t_α} correspond to loss in spatial domain, FFT domain and FRFT domain with parameter α , respectively. From Figure 3 (a) of main paper, they can be defined as,

$$\begin{aligned} \mathcal{L}_s &= \sum_{p=1}^3 \frac{1}{N_p} \|\hat{\mathbf{Y}}_p - \mathbf{Y}_p\|_1, \\ \mathcal{L}_{t_1} &= \sum_{p=1}^3 \frac{1}{N_p} \|\mathcal{F}(\hat{\mathbf{Y}}_p) - \mathcal{F}(\mathbf{Y}_p)\|_1, \\ \mathcal{L}_{t_\alpha} &= \sum_{p=1}^3 \frac{1}{N_p} \|\mathcal{F}_\alpha(\hat{\mathbf{Y}}_p) - \mathcal{F}_\alpha(\mathbf{Y}_p)\|_1, \end{aligned} \quad (16)$$

where, \mathbf{Y}_p is the scaled GT at p -th scale, N_p is number of elements for normalization at p -th scale, $\mathcal{F}(\cdot)$ is FFT operation and $\mathcal{F}_\alpha(\cdot)$ is FRFT operation with parameter α . λ_{t_1} and λ_{t_α} are weights corresponding to \mathcal{L}_{t_1} and \mathcal{L}_{t_α} , respectively. We empirically decide $\mathcal{L}_{t_1} = \mathcal{L}_{t_\alpha} = 0.1$ and $\alpha = 0.5$.

A.2. Parameter settings for training F2former

We adopt the training strategy of NAFNet [6] and FFT-former [17]. Specifically, adopting their data augmentation strategy and Adam optimizer with default values. Initial learning rate is set at 1×10^{-3} and is updated with cosine annealing upto 600,000 iterations. The minimum learning rate is set at 1×10^{-7} . F2former is trained with input images of shape $256 \times 256 \times 3$ with a batch size of 8. For computing self-attention we set the patch size as 8×8 . Other parameters like α for FRFT computation in FHTB block and λ as the cut-off frequency for cosine-bell function in FM-FFN

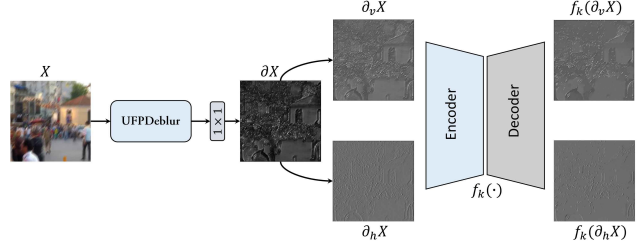


Figure 10. Workflow of our KEB module.

are set as learnable parameter and are updated during training based on minimizing the loss function. The corresponding details are discussed later in ablation section. All the experiments are carried out in a single 80GB Nvidia A100 GPU.

A.3. Kernel estimation block (KEB)

For a given blurry input \mathbf{X} , KEB estimates its corresponding blurry kernel \mathbf{K} . Its detail overflow is shown in Figure 10. Primarily, we use kernel estimation network from [14] where for each pixel the blur kernel is estimated of shape 19×19 . However, this kernel can not be used directly for Wiener deconvolution as it will increase the overall computation cost. Therefore, upon reshaping this estimated kernel, it turns out the gradient map ($\partial\mathbf{X}$) while also highlighting the blur pattern. To estimate an accurate blur kernel from $\partial\mathbf{X}$, we leverage the blur kernel estimation method in [49]. Basically, we estimate gradient at the vertical ($\partial_v\mathbf{X}$) and horizontal ($\partial_h\mathbf{X}$) direction from $\partial\mathbf{X}$ which is later passed to a 6-layer auto-encoder as shown in Figure 10. The encoder part removes unnecessary details of image gradients while the decoder extracts the major structural details with enhanced edges formulated as $\partial_v\mathbf{X}_e = f_K(\partial_v\mathbf{X})$ and $\partial_h\mathbf{X}_e = f_K(\partial_h\mathbf{X})$, where $f_K(\cdot)$ is auto-encoder operation as shown in above Figure. The design of auto-encoder as well as its training is carried out according to the respective details in [49].

After obtaining the salient edges as $\partial\mathbf{X}_e = f_K(\partial\mathbf{X})$ for blurry input \mathbf{X} , the blur kernel (\mathbf{K}) can be estimated from the following optimization problems,

$$\begin{aligned} \mathbf{K} &= \arg \min_{\mathbf{K}} \|\mathbf{K} \cdot \partial\mathbf{X}_e - \partial\mathbf{X}\|_2^2 + \eta \|\mathbf{K}\|_2^2, \\ \mathbf{X}_l &= \arg \min_{\mathbf{X}_l} \|\mathbf{K} \cdot \mathbf{X}_l - \mathbf{X}\|_2^2 + \gamma \|\mathbf{X}_l\|_2^2, \end{aligned} \quad (17)$$

where, η and γ are parameters for regularization terms, and \mathbf{X}_l is intermediate latent image. Similar to [49], we use \mathbf{X}_l to update the edge information in $\partial\mathbf{X}_e$. From [49], the closed form solution of the first optimization problem

Algorithm 1 An algorithm for estimating blur kernel \mathbf{K}

Require: Blurry input image \mathbf{X}

$\partial\mathbf{X} \leftarrow \text{Conv}_{1 \times 1}(\text{UFPdeblur}(\mathbf{X}))$
 $\partial_v\mathbf{X}, \partial_h\mathbf{X} \leftarrow \text{Sobel}(\partial\mathbf{X}) \quad \triangleright$ Sobel filter operation for
horizontal and vertical gradient extraction
 $\partial_v\mathbf{X}_e, \partial_h\mathbf{X}_e \leftarrow f_K(\partial_v\mathbf{X}), f_K(\partial_h\mathbf{X}) \quad \triangleright$ Autoencoder
operation
for $i = 1 : \tau$ **do**
 Solve for \mathbf{K} using equation 4
 Solve for \mathbf{X}_l using 2nd optimization in equation 3
 $\partial\mathbf{X}_l \leftarrow \text{Conv}_{1 \times 1}(\text{UFPdeblur}(\mathbf{X}_l))$
 $\partial\mathbf{X}_e \leftarrow \partial\mathbf{X}_l$
end for
return Estimated blur kernel \mathbf{K}

in equation 17 can be written in continuous domain as,

$$K = \mathcal{F}^{-1} \left(\frac{\overline{\mathcal{F}(\partial_h X_e)} \mathcal{F}(\partial_h X + \overline{\mathcal{F}(\partial_v X_e)} \mathcal{F}(\partial_v X))}{\mathcal{F}(\partial_h X_e)^2 + \mathcal{F}(\partial_h X_e)^2 + \eta} \right), \quad (18)$$

where $\mathcal{F}^{-1}(\cdot)$ is inverse FFT and $\overline{\mathcal{F}(\cdot)}$ is complex conjugate operation FFT domain. Then the kernel estimation can be formulated as per following algorithm

Here, the values of parameters η , γ , and τ are selected as 1, 0.002, and 15, respectively, according to [49]. Figure 11 shows the estimated kernel using the above algorithm as well as F2WD operation using this. Clearly, using the estimated kernel, F2WD is able to perform deblurring in latent space accurately. The accuracy of F2WD can be further improved if more accurate kernel estimation algorithm can be developed in feature space itself. We will investigate this further in future studies.

B. Proof of Proposition 1

The signal observation model in image domain can be written as,

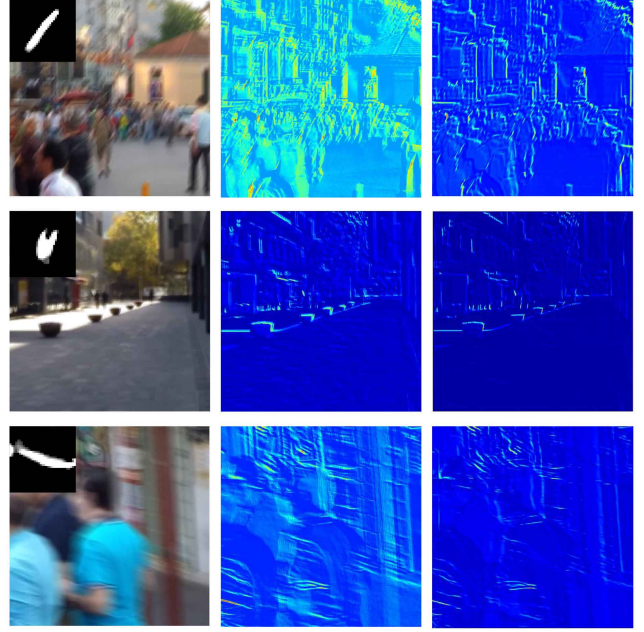
$$\mathbf{Y} = \mathbf{K}\mathbf{X} + \mathbf{n}, \quad (19)$$

where, \mathbf{Y} is observed data, \mathbf{X} is true signal, \mathbf{n} is associated noise elements and \mathbf{K} is the degradation process. Here, we consider the noise \mathbf{n} to be independent of input processes and is zero mean.

We assume that the Wiener deconvolution operator is \mathbf{G} in FRFT domain. Then, we can define the estimate of the true signal as,

$$\hat{\mathbf{X}} = \mathbf{F}^{-\alpha} \mathbf{C} \mathbf{G} \mathbf{F}^{\alpha} \mathbf{Y}, \quad (20)$$

where, \mathbf{C} corresponds to chirp multiplication with with diagonal elements $\mathbf{C}_{kk} = e^{-ik^2 \cot \theta / 2}$. This is included due to the convolution theorem in FRFT domain as shown in equation 8 (main paper). The design of filter or Wiener deconvolution operator is based on minimizing the mean



(a) Input with estimated PSF (b) \hat{X}_1^e w/o F2WD (c) \hat{X}_1^e w/ F2WD

Figure 11. Estimated Kernel for a given blurry image and visualization of F2WD operation using it. It is also compared with features without any Wiener deconvolution operation for proper understanding.

square error (MSE), which can be defined as following,

$$J_{\alpha} = \frac{1}{N} \mathbb{E}\{(\mathbf{X} - \hat{\mathbf{X}})^H (\mathbf{X} - \hat{\mathbf{X}})\} \quad (21)$$

Now, substituting equation 20 in above equation will result in

$$\begin{aligned}
J_{\alpha} &= \frac{1}{N} \mathbb{E}\{(\mathbf{X} - \mathbf{F}^{-\alpha} \mathbf{C} \mathbf{G} \mathbf{F}^{\alpha} \mathbf{Y})^H (\mathbf{X} - \mathbf{F}^{-\alpha} \mathbf{C} \mathbf{G} \mathbf{F}^{\alpha} \mathbf{Y})\} \\
&= \frac{1}{N} [\mathbb{E}\{\mathbf{X}^H \mathbf{X}\} - \mathbb{E}\{\mathbf{X}^H \mathbf{F}^{-\alpha} \mathbf{C} \mathbf{G} \mathbf{F}^{\alpha} \mathbf{Y}\} \\
&\quad - \mathbb{E}\{(\mathbf{F}^{-\alpha} \mathbf{C} \mathbf{G} \mathbf{F}^{\alpha} \mathbf{Y})^H \mathbf{X}\} \\
&\quad + \mathbb{E}\{(\mathbf{F}^{-\alpha} \mathbf{C} \mathbf{G} \mathbf{F}^{\alpha} \mathbf{Y})^H \mathbf{F}^{-\alpha} \mathbf{C} \mathbf{G} \mathbf{F}^{\alpha} \mathbf{Y}\}]
\end{aligned} \quad (22)$$

Now, we analyse each term in equation 22. For the first term $\mathbb{E}\{\mathbf{X}^H \mathbf{X}\}$, it suggest the autocorrelation matrix of true signal denoted as $\mathbf{S}^{xx} = \mathbb{E}\{\mathbf{X}^H \mathbf{X}\}$.

The second term can be re-written in terms of cross-correlation matrix between \mathbf{X} and \mathbf{Y} , which can be defined as, $\mathbf{S}^{xy} = \mathbb{E}\{\mathbf{X} \mathbf{Y}^H\}$. Hence, $\mathbb{E}\{\mathbf{X}^H \mathbf{F}^{-\alpha} \mathbf{C} \mathbf{G} \mathbf{F}^{\alpha} \mathbf{Y}\} = \mathbb{E}\{\mathbf{S}^{xy} \mathbf{F}^{-\alpha} \mathbf{C} \mathbf{G} \mathbf{F}^{\alpha}\}$.

Similarly the third term can be written as,

$$\mathbb{E}\{(\mathbf{F}^{-\alpha} \mathbf{C} \mathbf{G} \mathbf{F}^{\alpha} \mathbf{Y})^H \mathbf{X}\} = \mathbb{E}\{(\mathbf{F}^{-\alpha} \mathbf{C} \mathbf{G} \mathbf{F}^{\alpha})^H \mathbf{S}^{yx}\}. \quad (23)$$

For the last term, it can be simplified as following,

$$\begin{aligned} & \mathbb{E}\{(\mathbf{F}^{-\alpha}\mathbf{C}\mathbf{G}\mathbf{F}^{\alpha}\mathbf{Y})^H\mathbf{F}^{-\alpha}\mathbf{C}\mathbf{G}\mathbf{F}^{\alpha}\mathbf{Y}\} \\ &= \mathbb{E}\{\mathbf{Y}^H\mathbf{F}^{-\alpha}\mathbf{G}^H\mathbf{C}^H\mathbf{F}^{\alpha}\mathbf{F}^{-\alpha}\mathbf{C}\mathbf{G}\mathbf{F}^{\alpha}\mathbf{Y}\} \quad (24) \\ &= \mathbb{E}\{\mathbf{Y}^H\mathbf{F}^{-\alpha}\mathbf{G}^H\mathbf{G}\mathbf{F}^{\alpha}\mathbf{Y}\} \end{aligned}$$

In equation 24, the last line is from the properties of FRFT that $\mathbf{F}^{\alpha}\mathbf{F}^{-\alpha} = \mathbf{F}^{-\alpha+\alpha} = \mathbf{F}^0$, which is a unitary matrix. Similarly, $\mathbf{C}^H\mathbf{C} = \mathbf{I}$, due to the orthogonal properties of chirp function.

Now, as the \mathbf{G} consists of only diagonal elements, the equation 22 can be rewritten in terms of trace of the matrix. So, using the above expression, it can be reformulated as,

$$\begin{aligned} J_{\alpha} &= \frac{1}{N}[\text{tr}(\mathbf{S}^{xx}) - \text{tr}(\mathbf{S}^{xy}\mathbf{F}^{-\alpha}\mathbf{C}\mathbf{G}\mathbf{F}^{\alpha}) \\ &\quad - \text{tr}((\mathbf{F}^{-\alpha}\mathbf{C}\mathbf{G}\mathbf{F}^{\alpha})^H\mathbf{S}^{yx}) + \text{tr}(\mathbf{Y}^H\mathbf{F}^{-\alpha}\mathbf{G}^H\mathbf{G}\mathbf{F}^{\alpha}\mathbf{Y})], \quad (25) \end{aligned}$$

where, $\text{tr}(\cdot)$ is trace of matrix. Now, for each diagonal element of \mathbf{G}_j , we minimize J_{α} as following,

$$\frac{\partial J_{\alpha}}{\partial \mathbf{G}_j} = -(\mathbf{C}_{jj}\mathbf{F}_{jj}^{\alpha}\mathbf{S}_{jj}^{xy}\mathbf{F}_{jj}^{-\alpha})^H + \mathbf{F}_{jj}^{\alpha}\mathbf{S}_{jj}^{yy}\mathbf{F}_{jj}^{-\alpha}\mathbf{G}_j. \quad (26)$$

To minimize J_{α} , we have to make above equation 0, and then solving for \mathbf{G}_j we get,

$$\mathbf{G}_j = \frac{(\mathbf{C}_{jj}\mathbf{F}_{jj}^{\alpha}\mathbf{S}_{jj}^{xy}\mathbf{F}_{jj}^{-\alpha})^H}{\mathbf{F}_{jj}^{\alpha}\mathbf{S}_{jj}^{yy}\mathbf{F}_{jj}^{-\alpha}}, \quad (27)$$

where, \mathbf{S}^{yy} is auto-correlation of signal \mathbf{Y} , which can be defined as,

$$\begin{aligned} \mathbf{S}^{yy} &= \mathbb{E}\{\mathbf{Y}\mathbf{Y}^H\} = \mathbb{E}\{(\mathbf{K}\mathbf{X} + \mathbf{n})(\mathbf{K}\mathbf{X} + \mathbf{n})^H\} \\ &= \mathbb{E}\{\mathbf{K}\mathbf{X}\mathbf{X}^H\mathbf{K}^H\} + \mathbb{E}\{\mathbf{n}\mathbf{n}^H\} + \mathbb{E}\{\mathbf{n}\mathbf{X}^H\mathbf{K}^H\} \\ &\quad + \mathbb{E}\{\mathbf{X}\mathbf{K}\mathbf{n}^H\}. \quad (28) \end{aligned}$$

In above equation, $\mathbb{E}\{\mathbf{n}\mathbf{X}^H\mathbf{K}^H\} = \mathbb{E}\{\mathbf{X}\mathbf{K}\mathbf{n}^H\} = 0$, as \mathbf{X} and \mathbf{n} are independent. Now, as $\mathbf{S}^{nn} = \mathbb{E}\{\mathbf{n}\mathbf{n}^H\}$ and $\mathbf{S}^{xx} = \mathbb{E}\{\mathbf{X}\mathbf{X}^H\}$, we replace them in above equation to get

$$\mathbf{S}^{yy} = \mathbf{K}\mathbf{S}^{xx}\mathbf{K}^H + \mathbf{S}^{nn}. \quad (29)$$

Similarly, the cross correlation term \mathbf{S}^{xy} can be written as,

$$\begin{aligned} \mathbf{S}^{xy} &= \mathbb{E}\{\mathbf{X}\mathbf{Y}^H\} = \mathbb{E}\{\mathbf{X}(\mathbf{K}\mathbf{X} + \mathbf{n})^H\} \\ &= \mathbb{E}\{\mathbf{X}\mathbf{X}^H\mathbf{K}^H\} + \mathbb{E}\{\mathbf{X}\mathbf{n}^H\} = \mathbf{S}^{xx}\mathbf{K}^H. \quad (30) \end{aligned}$$

Now transferring equation 28 and 30 in equation 27, we will get the derived formulation in equation 7 (main paper). Hence, this completes the proof.

C. Ablation study (continued)

C.1. Effect of F3RB

We train our base model without F3RB which was added to extract features in terms of different contextual information with respect to varied α parameter for FRFT operation. We observe a 0.13 dB drop in PSNR compared to our baseline performance.

C.2. Visualization of learnable α for FRFT in F2WD and FHTB

In all FRFT operations in F2former, we have taken the α parameter as learnable parameter, specifically, we set $\alpha = \{\alpha_x, \alpha_y\}$ to apply FRFT in horizontal and vertical directions of an image separately. The main reason behind this is that based on different blur content at different scales there would be separate requirement of α parameters to represent optimal spatial-frequency information. It also depends on specific task of the block like the role of FHTB blocks in encoder side is different compared to that of decoder side (encoder part minimizes the blur content at different scales, whereas the decoder part efficiently reconstructs the sharp image details). This can be visualized from Figure 12 where each plot represent the average α variation with respect to training iterations and corresponding to a particular FHTB block at particular scale. Usually, for encoder operations α varies between (0.4, 0.7), whereas for decoder operation it varies between (0.1, 0.7). Our hypothesis is that as decoder (specially at last stage) mainly focuses on reconstructing the sharp image details, it majorly focuses on the spatial content of the image making it low α values as shown in last plot of Figure 12. It is also noticeable from the above figure that α also varies across horizontal and vertical directions. This is mostly due to focus on different important gradient information at separate scales and separate levels (encoder or decoder).

Figure 13 shows the α variation to perform featured based fractional Wiener deconvolution at different scales. As at downsampled level, the spatially varying blur dominates more, we see more focus of F2WD to spatial content (low α values) as the model gets deeper. Due to this optimal choice of α , F2WD is able to perform feature based deblurring operation more effectively as shown in Figure 11. For further verification, we retrain our model with fixed $\alpha = 0.5$ for both horizontal and vertical direction as suggested by [52] for both F2WD and FSGT. We observe a 0.18 dB reduced PSNR compared to our baseline performance.

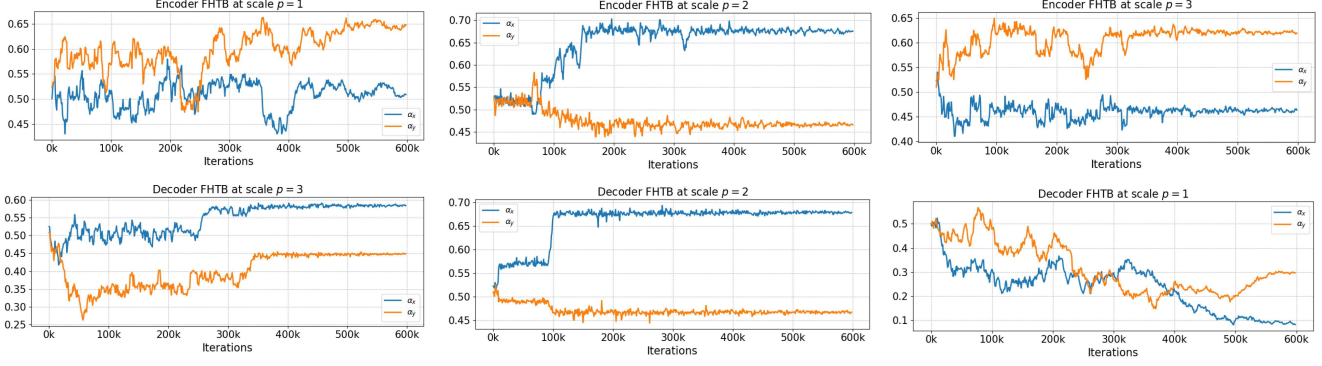


Figure 12. Visualization of variation of α for FRFT operations in FHTBs at different scales of F2former base model

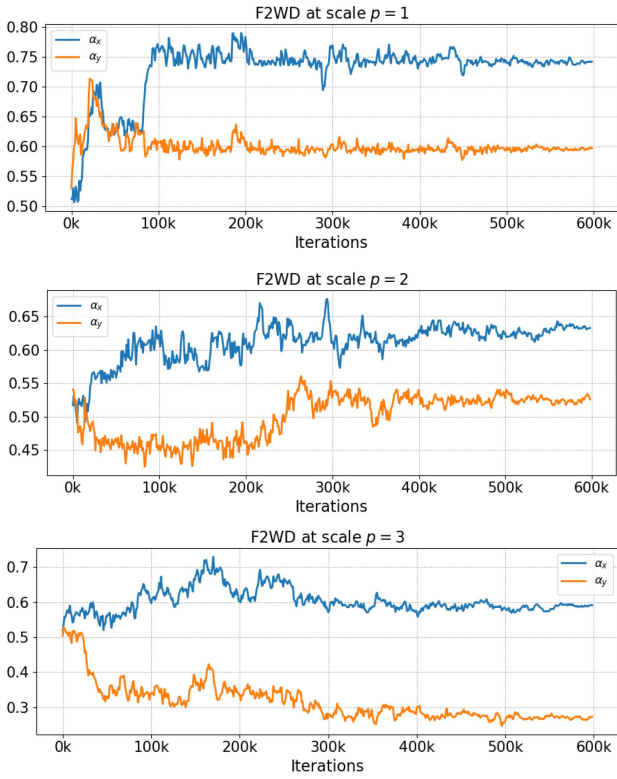


Figure 13. Visualization of variation of α for FRFT operations in F2WDs at different scales of F2former base model

C.3. Effect of Cosine-bell function in FM-FFN

The cosine bell formulation in equation 13 (main paper) is generic. The exact formulation is defined as below,

$$\mathbf{W}_{jk}^l = \begin{cases} 1 & \text{if } |u| \leq u_c - \frac{u_s}{2} \\ 0.5 \left[1 + \cos \left(\frac{\pi(|u| - u_c + \frac{u_s}{2})}{u_s} \right) \right] & \text{if } \lambda_{ls} < |u| < \lambda_{rs} \\ 0 & \text{if } |u| \geq u_c + \frac{u_s}{2}, \end{cases} \quad (31)$$

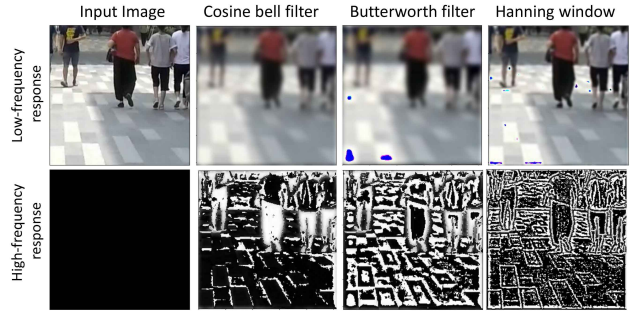


Figure 14. Visualization of extracted low-pass and high-pass image signal using different filters.

where, $\lambda_{ls} = u_c - \frac{u_s}{2}$, $\lambda_{rs} = u_c + \frac{u_s}{2}$, and $u = \sqrt{j^2 + k^2}$. So, threshold λ in equation 13 is basically consists of two parameters, u_c which is cut-off frequency and u_s which is pass band frequency to reduce ringing effect in spatial domain. Figure 14 shows the advantage of using cosine bell function compared to other formulations like butterworth and hanning window operation. Clearly cosine bell reduces the ringing artifacts and reconstructs high and low frequency images more effectively for same cut-off frequency.

We keep both u_c and u_s as the learning parameter during training our network. Figure 15 shows the variation of u_c and u_s across the training iterations. For optimal high and low frequency extraction, the cut-off frequency for all FHTB blocks varies between (8,12) in saturation whereas to reduce the ringing effect the pass band frequency mainly varies in (24,34) across all the FHTBs. For further validation we use the three filters shown in Figure 14 for training upto 200k iterations on GoPro dataset. The respective test results are shown in Table 5. Clearly, the utilization of cosine bell function as a filter benefits our proposed F2former compared to other filters.

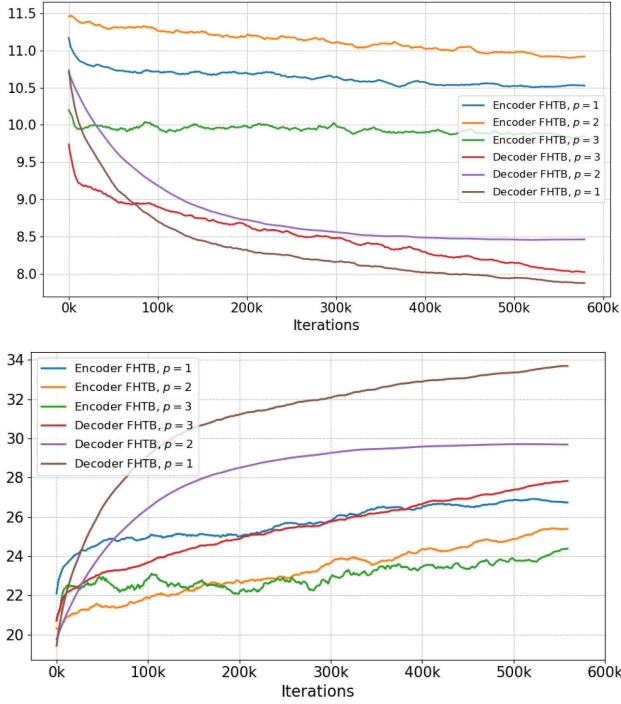


Figure 15. Variation of u_c (top) and u_s (bottom) across the training iterations.

Table 5. Effect of different filters on the performance of F2former

Filters	PSNR	SSIM
Cosine Bell	33.24	0.961
Butterworth	33.02	0.953
Hanning window	33.11	0.957

C.4. Visualization of effect of FM-FFN

Figure 16 shows how FM-FFN extracts high and low frequency features, and based on important frequency information it generates sharp details as shown in the Figure. Clearly, compared to before FFN features, the features after FFN has more sharper edges and more structural details.

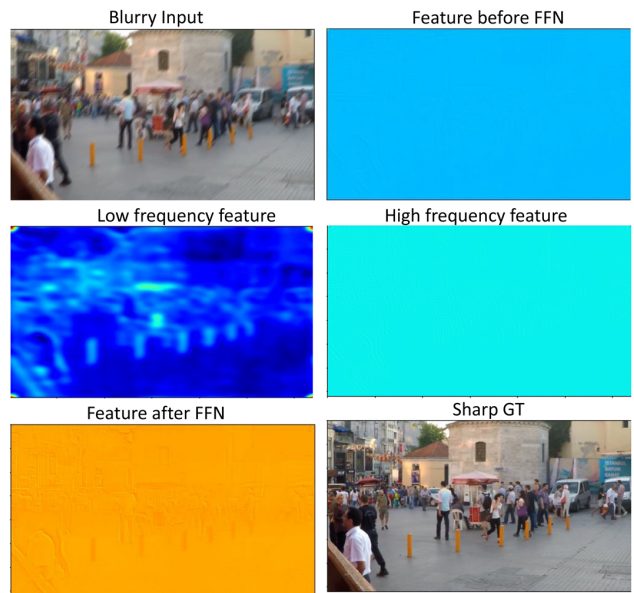


Figure 16. Visualization of extracted low and high frequency features in FM-FFN of last F2TB block (better visualized in 200-300%)

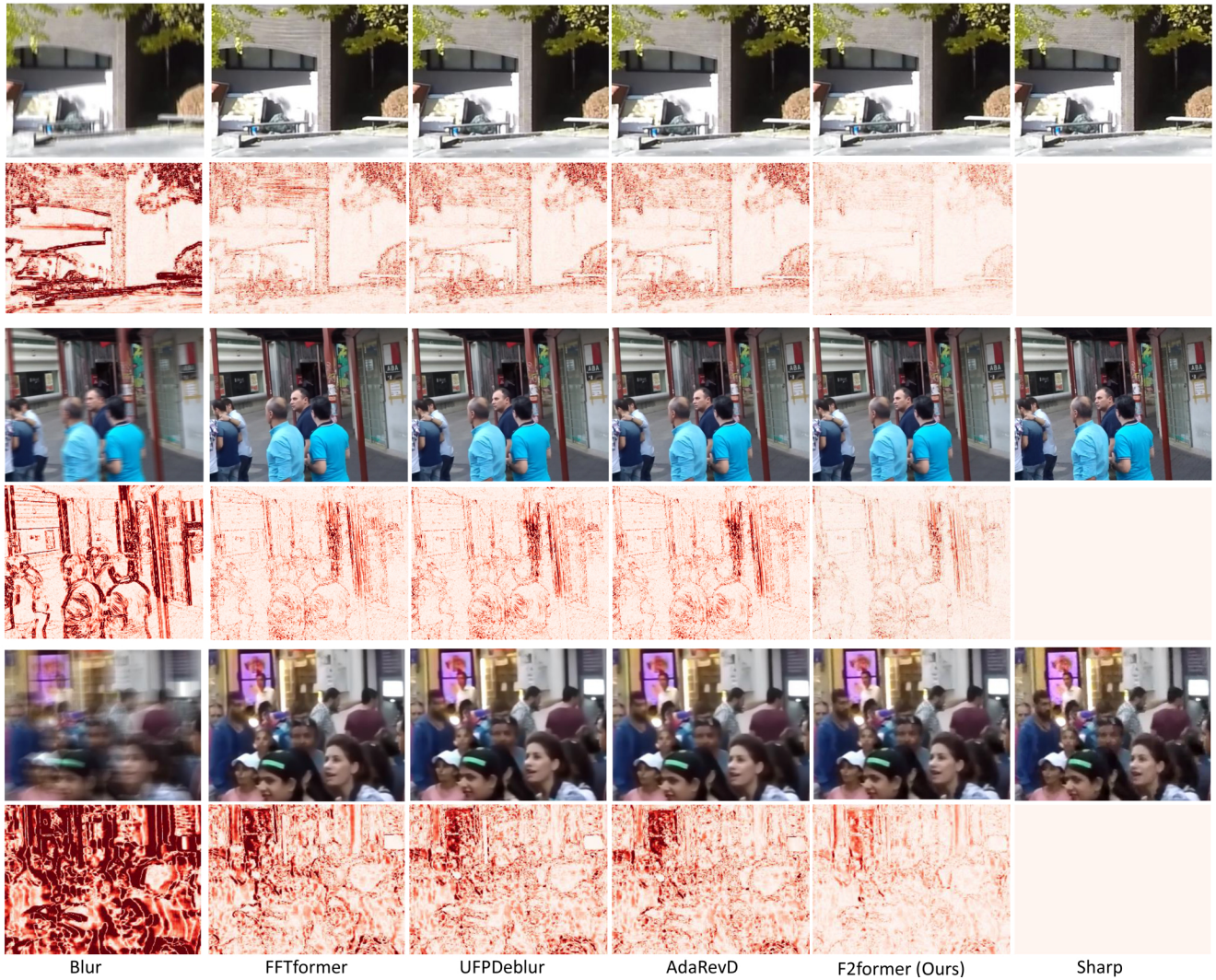


Figure 17. Examples on the GoPro test dataset. The odd rows show blur image, predicted images of different methods, and GT sharp image. The even rows show the corresponding residual of the blur image / predicted sharp images and GT sharp image. Better visualized at 200%.

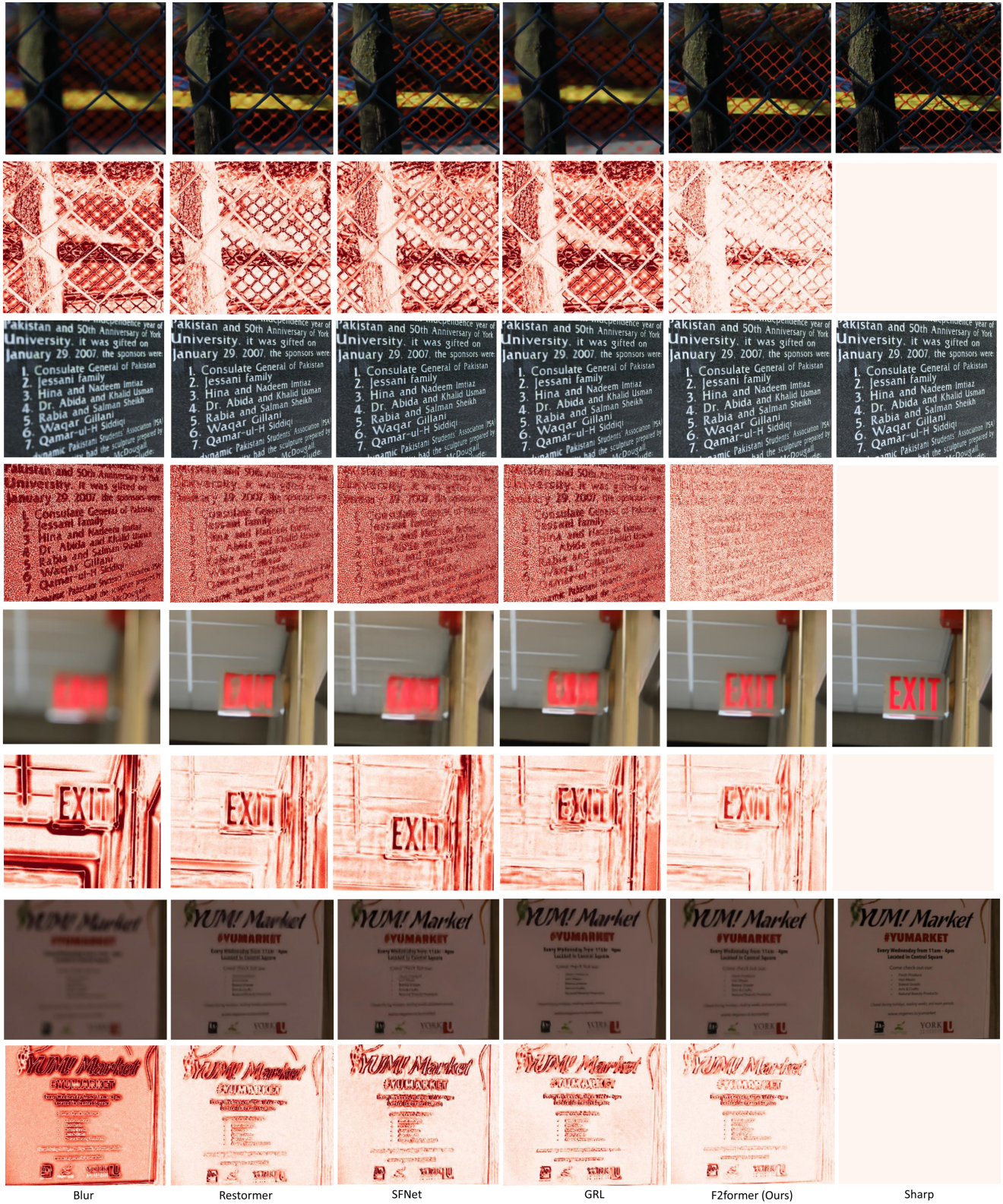


Figure 18. Examples on the DDPD-single pixel test dataset. The odd rows show blur image, predicted images of different methods, and GT sharp image. The even rows show the corresponding residual of the blur image / predicted sharp images and GT sharp image. Better visualized at 200%.



Figure 19. Examples on the DDPD-dual pixel test dataset. The odd rows show blur image, predicted images of different methods, and GT sharp image. The even rows show the corresponding residual of the blur image / predicted sharp images and GT sharp image. Better visualized at 200%.

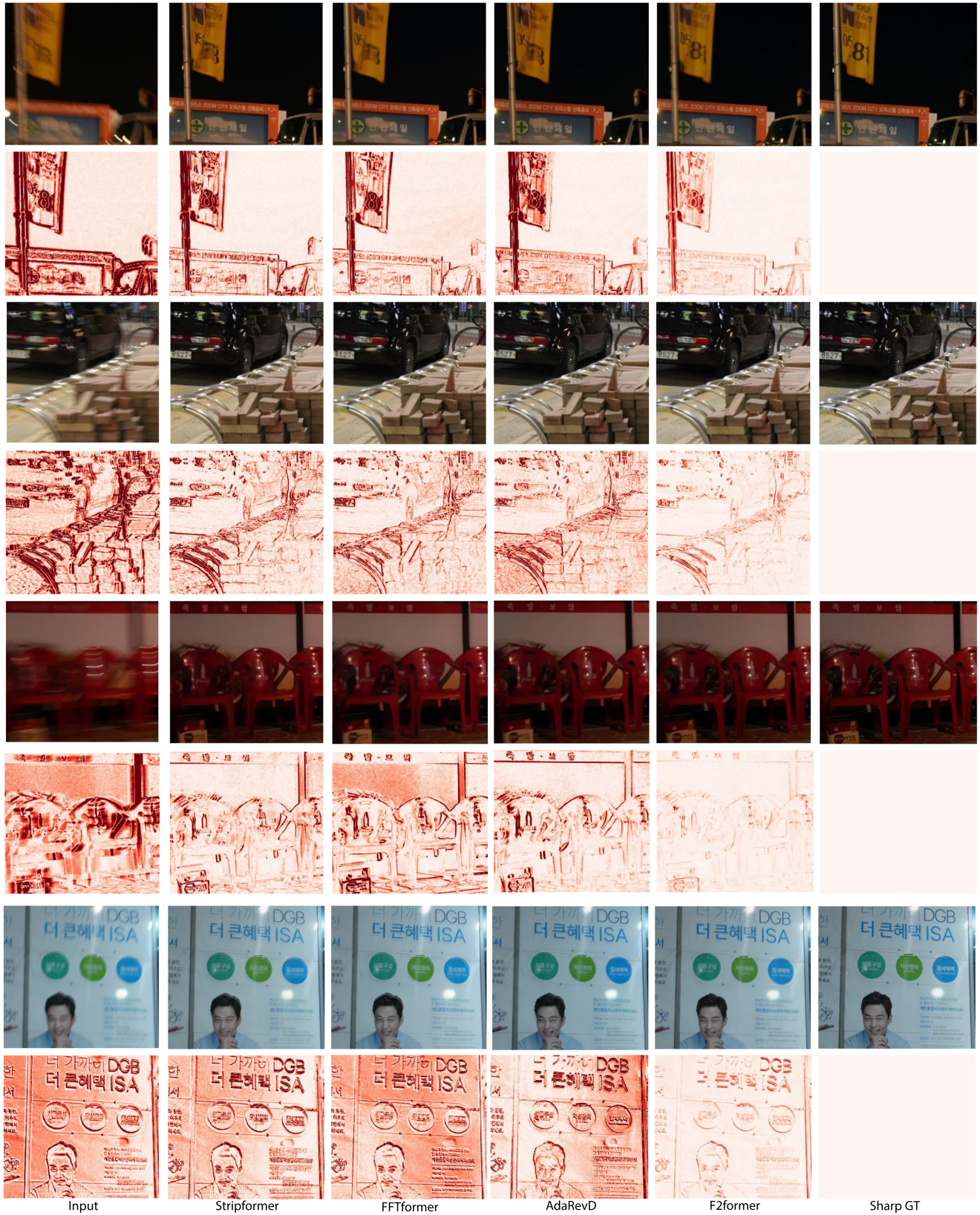


Figure 20. Examples on the RealBlur-J test dataset. The odd rows show blur image, predicted images of different methods, and GT sharp image. The even rows show the corresponding residual of the blur image / predicted sharp images and GT sharp image. Better visualized at 200%.

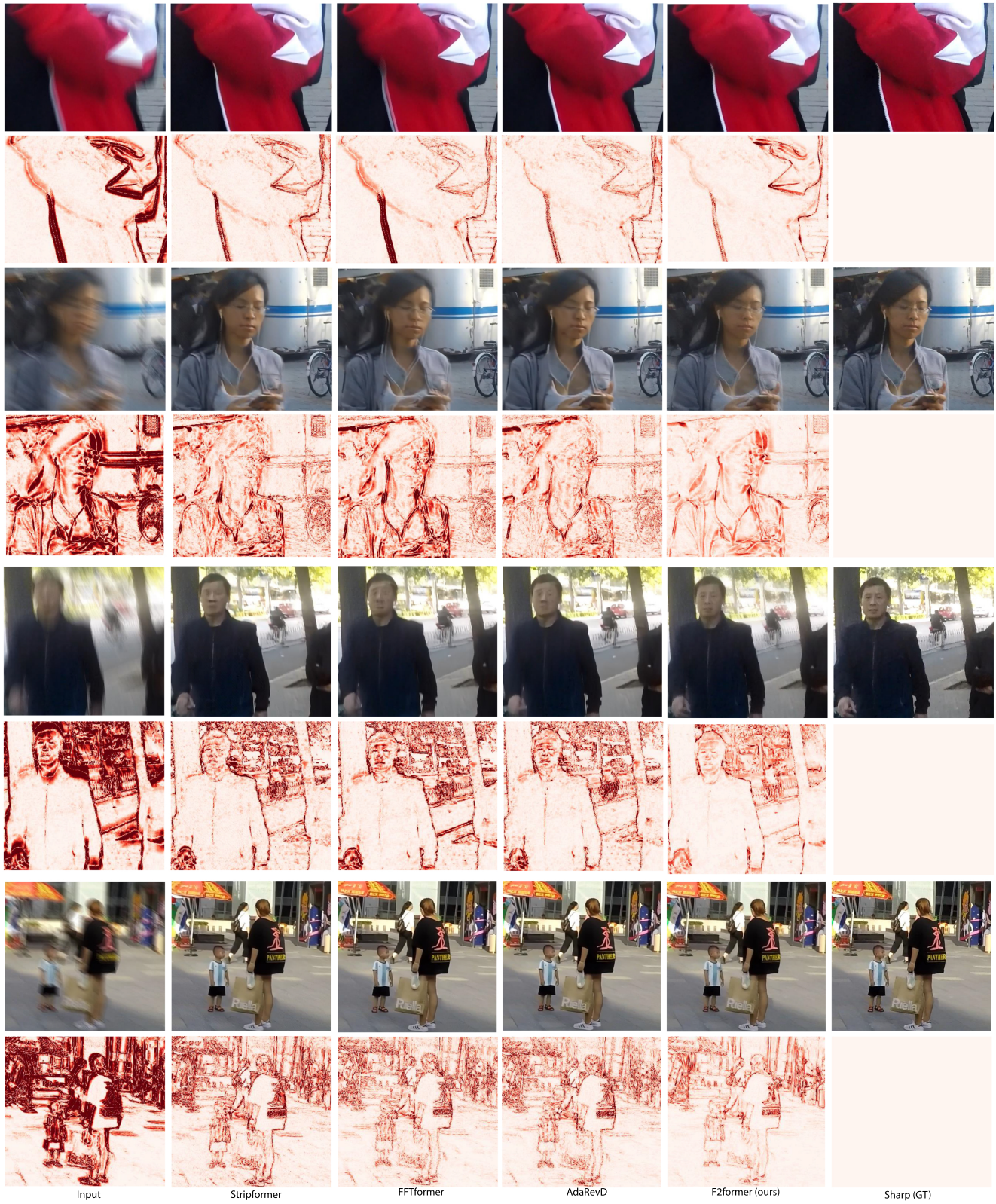


Figure 21. Examples on the HIDE test dataset. The odd rows show blur image, predicted images of different methods, and GT sharp image. The even rows show the corresponding residual of the blur image / predicted sharp images and GT sharp image. Better visualized at 200%.